

1 **Earthquake-induced landslides in Haiti: analysis of**  
2 **seismotectonic and possible climatic influences**

3

4 Hans-Balder Havenith<sup>1</sup>, Kelly Guerrier<sup>2</sup>, Romy Schlögel<sup>1,3</sup>, Anika Braun<sup>4</sup>, Sophia  
5 Ulysse<sup>2,5</sup>, Anne-Sophie Mreyen<sup>6</sup>, Karl-Henry Victor<sup>2</sup>, Newdeskarl Saint-Fleur<sup>2</sup>, Lena  
6 Cauchie<sup>1</sup>, Dominique Boisson<sup>2</sup>, Claude Prépetit<sup>5</sup>

7

8 <sup>1</sup>University of Liege, Department of Geology, Georisk and Environment, Liege, 4000, Belgium

9 <sup>2</sup>Université d'Etat d'Haïti, Faculté des Sciences, LMI-CARIBACT, URGéo, Port-au-Prince, Haiti

10 <sup>3</sup>Centre Spatial de Liège, Liege, 4000, Belgium

11 <sup>4</sup>TU Berlin, Faculty VI Planning Building, Environment Department of Engineering Geology, Berlin,  
12 1587, Germany

13 <sup>5</sup>Unité Technique de Sismologie, Bureau des Mines et de l'Energie, Port-au-Prince, Delmas 31, Haiti

14 <sup>6</sup>University of Liege, Department of Urban & Environmental Engineering, Applied Geophysics, Liege,  
15 4000, Belgium

16

17 Correspondence to: Hans-Balder Havenith ([hb.havenith@uliege.be](mailto:hb.havenith@uliege.be))

18

19

20

21

22

23

24 **Abstract.** First analyses of landslide distribution and triggering factors are presented for the region  
25 affected by the August, 14, 2021, earthquake (Mw=7.2) in the Nippes Department, Haiti. Landslide  
26 mapping was mainly carried out by comparing pre- and post-event remote imagery (~0.5 -1-m resolution)  
27 available on Google Earth Pro® and Sentinel-2 (10-m resolution) satellite images. The first covered  
28 about 50% of the affected region (for post-event imagery and before completion of the map in January  
29 2022), the latter were selected to cover the entire potentially affected zone. On the basis of the completed  
30 landslide inventory, comparisons are made with catalogues compiled by others both for the August 2021  
31 and the January 2010 seismic events, including one open inventory (by the United States Geological  
32 Survey) that was also used for further statistical analyses. Additionally, we studied the pre-2021  
33 earthquake slope stability conditions. These comparisons show that the total number of landslides  
34 mapped for the 2021 earthquake (7091) is larger than the one recently published by another research  
35 team for the same event, but [slightly smaller than the number of landslides mapped by a third research](#)  
36 [team.](#) It is also clearly smaller than the one observed by two other research teams for the 2010 earthquake  
37 (e.g., 23,567, for the open inventory). However, these apparently fewer landslides triggered in 2021 cover  
38 much wider areas of slopes (>80 km<sup>2</sup>) than those induced by the 2010 event (~25 km<sup>2</sup> – considering the  
39 open inventory). A simple statistical analysis indicates that the lower number of 2021-landslides can be  
40 explained by the missing detection of the smallest landslides triggered in 2021, partly due to the lower  
41 resolution imagery available for most of the areas affected by the recent earthquake; this is also confirmed  
42 by an inventory completeness analysis based on size-frequency statistics. The much larger total area of  
43 landslides triggered in 2021, compared to the 2010 earthquake, can be related to different physical  
44 reasons: a) the larger earthquake magnitude in 2021; b) the more central location of the fault segment  
45 that ruptured in 2021 with respect to coastal zones; c) and possible climatic preconditioning of slope  
46 instability in the 2021-affected area. These observations are supported by (1) a new pre-2021 earthquake  
47 landslide map, (2) rainfall distribution maps presented for different periods (including October 2016 -  
48 when Hurricane Matthew had crossed the western part of Haiti), covering both the 2010 and 2021  
49 affected zones, as well as (3) shaking intensity prediction maps.

## 50 1 Introduction

51 This paper presents ~~an first~~ overview of landslides induced by the August 14, 2021, Nippes (Haiti)  
52 earthquake. The epicenter (18.434° N / 73.482° W, hypocentral depth of 10 km) of this event is located  
53 in the western part of the southern Haitian peninsula (see Unites States Geological Survey, USGS,  
54 Earthquake Hazard Program page, [earthquake.usgs.gov](https://earthquake.usgs.gov), presenting first information on the 2021 M 7.2  
55 - Nippes, Haiti, event).

56 Even though the magnitude of the 2021 earthquake is slightly larger than the one of 2010 (Mw=7.2 and  
57 Mw=7.0, respectively, see information on the earthquake.usgs.gov webpage and by Stein et al., 2021),  
58 the recent event was far less catastrophic as it hit a less populated area compared to the 2010 earthquake  
59 that occurred just near the western entrance of the capital of Haiti, Port-au-Prince. The 2021 earthquake  
60 accounts for about 2250 fatalities (2/3 of which occurred in the provincial city of Les Cayes, located in  
61 Fig. 1), while the 2010 death toll is up to 300.000. However, it quickly became clear that the last event  
62 caused widespread slope failures that could be more intense than in 2010. Therefore, members of our  
63 research team completed some ground control during a one-week field visit along segments of important  
64 roads hit by rock falls near the epicentral region. Additionally, we mapped landslides over the whole area  
65 potentially hit by the 2021 event by using satellite imagery of variable resolution, as it will be explained  
66 in section 3. The main target of this mapping task was to produce an input data set for an extensive  
67 landslide susceptibility analysis that will be presented in an upcoming publication.

68 Such event-based seismically induced landslide inventories also allow us to complete a more systematic  
69 analysis of global patterns of those mass movements, such as size-frequency relationships (Malamud et  
70 al., 2004; Tanyas et al., 2019b), estimates of the expected number of landslides and affected area  
71 (Havenith et al., 2016; Keefer and Wilson, 1989; Marc et al., 2017), and very general earthquake-  
72 triggered landslide susceptibility markers (Tanyas et al., 2019a). At regional scale, event-based landslide  
73 inventories are valuable to understand more specific patterns of seismic slope instability, particularly  
74 with respect to the earthquake mechanism and the geological and climatic context (Gorum et al., 2011;  
75 Tanyas et al., 2022).

76 Below, we will also present statistical characteristics of this new 2021 inventory compared with  
77 equivalent results extracted from the USGS landslide catalogue published by Harp et al. (2016) for the

78 2010 Haiti event that occurred at about 100 km in the east of the 2021 earthquake. Some statistical data  
79 are also compared with those of two other published inventories completed for the 2021 event, the one  
80 by Martinez et al. (2021, USGS Open File report) and the one by Zhao et al. (2022) as well as with those  
81 of two additional catalogues compiled for the 2010 event (by Gorum et al., 2013 and Xu et al., 2014).  
82 The tectonic setting of both events and also the climatic context of the landslide triggering are introduced  
83 in the following section.

84 ~~Similar to the January 12, 2010, earthquake, the epicenter is located near the surface expression of the~~  
85 ~~Enriquillo Plantain-Garden Fault (EPGF) that crosses the peninsula from east to west, marking one of~~  
86 ~~the highest seismic hazard zones of the island (see location of the epicenters on the seismic hazard map~~  
87 ~~completed by Frankel et al. in 2011 in Fig. A1 in the annex, as well as on the topographic map shown in~~  
88 ~~Fig. 1).~~

89 ~~For the 2010 event, Calais et al. (2010) and Symithe et al. (2013) showed that this earthquake was caused~~  
90 ~~by the oblique rupture of a formerly unknown fault dipping towards the north and located immediately~~  
91 ~~in the north of the EPGF. Data provided by the [earthquake.usgs.gov](http://earthquake.usgs.gov) webpage (considering the provided~~  
92 ~~moment tensor solution; see also Okuwaki and Fan, 2022) indicate that the situation could be similar for~~  
93 ~~the 2021 event, with a ruptured fault segment dipping towards the north, and mostly located in the north~~  
94 ~~of the EPGF. Thus, also the recently ruptured fault segment would not belong to the EPGF (which is~~  
95 ~~essentially a left-lateral strike-slip fault). It could be related to an adjacent blind fault segment with~~  
96 ~~oblique slip character (left lateral strike slip combined with reverse movement) according to the~~  
97 ~~information available on [earthquake.usgs.gov](http://earthquake.usgs.gov), and to Okuwaki and Fan (2022). The latter further indicate~~  
98 ~~that especially the eastern part of the ruptured fault showed a more reverse while the western part a~~  
99 ~~preferential strike-slip mechanism. However, by now there is still no clear answer to the question related~~  
100 ~~to the fault itself. Therefore, below we will use the term of the ‘EPGF zone’ that includes the main strike-~~  
101 ~~slip fault and annexed oblique (or combined) slip fault segments (the two that are now known, i.e., the~~  
102 ~~one ruptured in 2010 and the one that produced the last earthquake) to denominate the tectonic structure~~  
103 ~~that produced those two events.~~

104 **2 Regional data and context of the earthquake-triggered landslides**

105 Similar to the January 12, 2010, earthquake, the epicenter of the main shock of the 2021 event is located

106 near the surface expression of the– Enriquillo-Plantain-Garden Fault (EPGF) that crosses the southern

107 peninsula from east to west west to east; this fault includes a succession of faulted anticlines forming the

108 Massif de la Hotte mountains in the west (zone affected by the 2021 event) and the Massif de la Selle in

109 the east (affected by the 2010 event); marking one of the highest seismic hazard zones of the island (see

110 location of the epicenters on the seismic hazard map completed by Frankel et al. in 2011 in Fig. A1 in

111 the annex, as well as on the topographic map shown in Fig. 1). With a slip rate of about  $7\pm 2$  mm yr<sup>-1</sup> the

112 EPGF is one of the two main strike-slip faults inferred to accommodate the 20 mm yr<sup>-1</sup> relative motion

113 between the Caribbean and North American plates (DeMets et al., 2000). Furthermore, the historical

114 earthquakes of 1701, 1751 and 1770 are considered to have occurred along the central EPGF system (Ali

115 et al., 2008; Bakun et al., 2012). Thus, EPGF marks one of the highest seismic hazard zones of the island

116 (see location of the recent epicenters on the seismic hazard map completed by Frankel et al. in 2011 in

117 Fig. A1 in the annex, as well as on the topographic map shown in Fig. 1).

118 For the 2010 event, Calais et al. (2010) and Symthe et al. (2013) showed that this earthquake was caused

119 by the oblique rupture of a formerly unknown fault (called ‘Léogane’) dipping towards the north and

120 located immediately in the north of the EPGF. Data provided by the earthquake.usgs.gov webpage

121 (considering the provided moment tensor solution; see also Okuwaki and Fan, 2022) indicate that the

122 situation could be similar for the 2021 event, with a ruptured fault segment dipping towards the north,

123 and mostly located in the north of the EPGF. Thus, also the recently ruptured fault segment would not

124 belong to the EPGF (which is essentially a left-lateral strike-slip fault). It could be related to an adjacent

125 blind fault segment with oblique slip character (left-lateral strike-slip combined with reverse movement)

126 according to the information available on earthquake.usgs.gov, and to Okuwaki and Fan (2022). The

127 latter further indicate that especially the eastern part of the ruptured fault showed a more reverse while

128 the western part a preferential strike-slip mechanism. However, by now there is still no clear answer to

129 the question related to the fault itself. Therefore, below we will use the term of the ‘EPGF zone’ that

130 includes the main strike-slip fault and annexed oblique (or combined) slip fault segments (the two that

131 are now known, i.e., the one ruptured in 2010 and the one that produced the last earthquake) to

Formatted: Font: (Default) Times New Roman, 10 pt

Formatted: Heading 1, Indent: Left: 0", First line: 0", Space Before: 24 pt, After: 12 pt, Outline numbered + Level: 1 + Numbering Style: 1, 2, 3, ... + Start at: 1 + Alignment: Left + Aligned at: 0.25" + Indent at: 0.5"

Formatted: Font: (Default) Times New Roman, 10 pt

Formatted: Font: Italic

Formatted: Font: Italic

Formatted: Font: (Default) Times New Roman, 10 pt, Not Highlight

Formatted: Font: (Default) Times New Roman, 10 pt

Formatted: Font: (Default) Times New Roman, 10 pt

Formatted: Font: (Default) Times New Roman, 10 pt, Not Highlight

Formatted: Font: (Default) Times New Roman, 10 pt

Formatted: Font: (Default) Times New Roman, 10 pt, Not Highlight

Formatted: Font: Italic

132 denominate the tectonic structure that produced those two events.

133 Even though the magnitude of the 2021 earthquake is slightly larger than the one of 2010 (Mw=7.2 and  
134 Mw=7.0, respectively, see information on the [earthquake.usgs.gov](https://earthquake.usgs.gov) webpage and by Stein et al., 2021);  
135 the recent event was far less catastrophic as it hit a less populated area compared to the 2010 earthquake  
136 that occurred just near the western entrance of the capital of Haiti, Port-au-Prince. The 2021 earthquake  
137 accounts for about 2250 fatalities (2/3 of which occurred in the provincial city of Les-Cayes, located in  
138 Fig. 1), while the 2010 death toll is up to 300,000. However, it quickly became clear that the last event  
139 caused widespread slope failures that could be more intense than in 2010. Therefore, members of our  
140 research team completed some ground control during a one-week field visit along segments of important  
141 roads hit by rock falls near the epicentral region. Additionally, we mapped landslides over the whole area  
142 potentially hit by the 2021 event by using satellite imagery of variable resolution, as it will be explained  
143 in section 2. The main target of this mapping task was to produce an input data set for an extensive  
144 landslide susceptibility analysis that will be presented in an upcoming publication.

145 Such event-based seismically induced landslide inventories allow us to complete a more systematic  
146 analysis of global patterns of those mass movements, such as size-frequency relationships (Malamud et  
147 al., 2004; Tanyas et al., 2019b), estimates of the expected number of landslides and affected area  
148 (Havenith et al., 2016; Keefer and Wilson, 1989; Marc et al., 2017), and very general earthquake-  
149 triggered landslide susceptibility markers (Tanyas et al., 2019a). At regional scale, event-based landslide  
150 inventories are valuable to understand more specific patterns of seismic slope instability, particularly  
151 with respect to the earthquake mechanism and the geological and climatic context (Gorum et al., 2011;  
152 Tanyas et al., 2022). Below, we will also present statistical characteristics of this new 2021 inventory  
153 compared with equivalent results obtained for the 2010 USGS landslide catalogue published by Harp et  
154 al. (2016); some statistical data are also compared with those of the other inventory completed by  
155 Martinez et al. (2021, USGS Open File report) for the 2021 event and of two additional catalogues  
156 compiled for the 2010 event (by Gorum et al., 2013 and Xu et al., 2014).

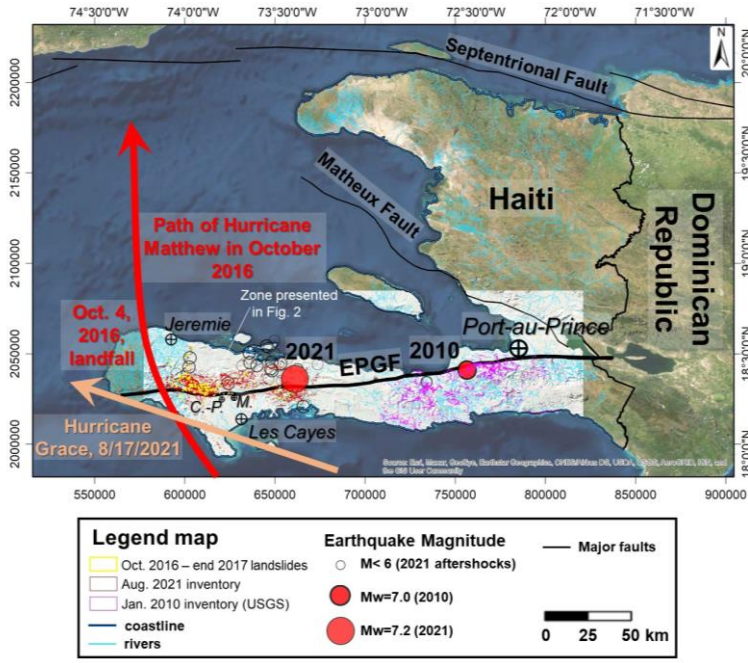
157 The seismotectonic setting of the two events in 2010 and 2021 introduced above has certainly to be  
158 considered when explaining observed earthquake-triggered landslide distributions (see sections 4 and 5  
159 below). However, also geological and climatic factors need to be analyzed to improve related  
160 interpretations. The geological influence on slope failure development in the earthquake-affected zones

161 will be studied more in detail in a follow-up paper focused on landslide susceptibility analyses (see also  
162 Zhao et al., 2022, for a basic analysis of the geological influence on the 2021 landslide distribution),  
163 while some possible climatic influence is already investigated in this paper. Finally, Therefore, we had  
164 also mapped landslides existing before the 2021 earthquake by using high-resolution (<=1 m) imagery  
165 available on Google Earth Pro®, starting from October 2014 until the end of 2017, to study some  
166 preconditioning of slope instability that was induced in 2021. In particular, it is known that the region is  
167 often affected by hurricanes – the last catastrophic one, ‘Matthew’ or ‘*Mathieu*’ in French, had impacted  
168 the target area in October 2016. ~~Also~~In addition, just two days after the main shock, on August 16,  
169 another Hurricane, ‘Grace’, hit the area and hampered help convoys to reach the areas most impacted by  
170 the earthquake. Right after this event, it was not immediately clear if Grace had contributed to landslide  
171 activity or not; this question will be analyzed in the following sections by comparing landslide  
172 distributions with monthly precipitation maps produced by the ‘Global Precipitation Measurement’  
173 (GPM) Mission (NASA) for different periods.

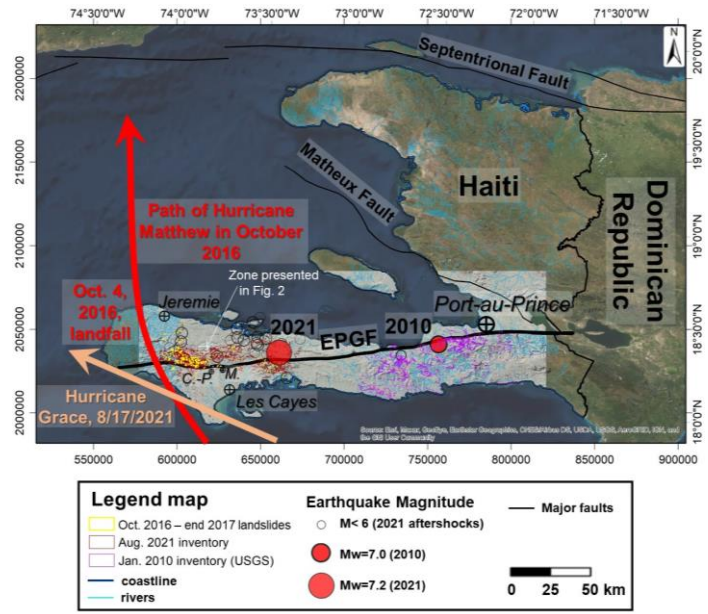
174 Fig. 1 presents an overview map with outlines of landslides mapped by Harp et al. (2016) (shown by  
175 light violet - pink polygons, near the 2010 M=7 epicenter), and the recently mapped landslides triggered  
176 in August 2021 (outlined in dark red, mainly in the west and south of the 2021 epicenter). This map also  
177 shows the approximate paths of the two aforementioned hurricanes near Haiti. Other digital outlines (also  
178 those presented in the following figures that also present more detailed views with more clearly visible  
179 outlines), such as roads, rivers, faults and coastline, were provided by the Centre National de  
180 l'Information Géo-Spatiale (CNIGS) of Haiti.

**Formatted:** Font: (Default) Times New Roman, 10 pt

**Formatted:** Normal, Space Before: 0 pt, After: 0 pt



181



182

183

Formatted: Normal, Space Before: 0 pt, After: 0 pt



184 **Figure 1: Location of the study region in Haiti: Satellite image view of Haiti (by © ESRI), with study region**  
185 **highlighted by the hillshade. See also location of the 2010 and 2021 epicenters, and the major cities (see also**  
186 **‘C.-P.’ for Camp-Perrin and ‘M.’ for Maniche) by hit by those two events. Outlines of major faults are shown**  
187 **as well as the indication of the approximate paths of Hurricane Matthew in October 2016 and of Hurricane**  
188 **Grace in August 2021. Landslides mapped by Harp et al. (2016) are shown by light violet polygons, and**  
189 **recently mapped landslides triggered in August 2021 are outlined in dark red See also location of the zone**  
190 **presented in Fig. 2.**

**Formatted:** Font: (Default) Times New Roman, 9 pt, Bold

191

192 The following sections will provide more detail about the landslide mapping itself, the completion of  
193 landslide statistics, the collection of climatic data and the computation of seismic intensity maps. All  
194 those inputs will be used to explain both the common and the different main markers of landslide  
195 catalogues, respectively, for the 2010 and the 2021 events.

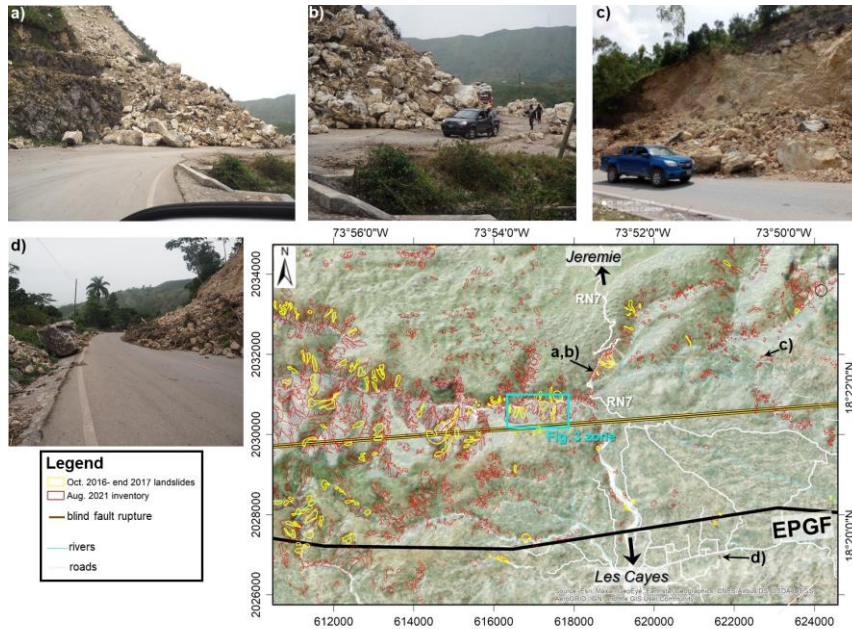
**Formatted:** Font: (Default) Times New Roman, 9 pt

## 196 2.3 **Methodological aspects of landslide and seismic trigger factor mapping**

### 197 **3.2.1 Landslide mapping**

#### 198 **3.2.1.1 Field observations**

199 Right after the main shock that hit Haiti on August 14, 2021 (precisely at 12:29:08 UTC, about 8:30 am  
200 local time), it became clear that many landslides were triggered by this earthquake. Within a few hours  
201 after the main shock, there were reports about rock falls cutting the main road RN7 connecting the large  
202 provincial cities of Les Cayes in the south and Jeremy in the north. Therefore, local members of our  
203 research team checked the situation to support local administration with cleaning the roads. Photographs  
204 of rock falls in the central part of the target area are shown in Fig. 2 (those shown below all occurred in  
205 limestone rocks), together with the locations of the affected sites on a map. \_-



206  
 207 **Figure 2: Examples of landslides photographed in the field, especially along the national road RN7, connecting**  
 208 **the two provincial cities of Les Cayes in the south and Jeremie in the north. The map (semi-transparent**  
 209 **hillshade on high-resolution satellite imagery, by © ESRI) also shows the different ground failure effects**  
 210 **mapped before (yellow polygons) and after the earthquake (dark red polygons). See blue rectangle marking**  
 211 **the outline of the view extent shown in Fig. 3 (and in Fig. A2).**

212  
 213 These rock falls were typically not very large (with a volume of generally less than 20,000 m<sup>3</sup> –note. for  
 214 volume estimates, we applied the equations proposed by Havenith et al., 2015, using as input the  
 215 landslide deposit thickness calculations and surface area measurements), but there were many of them  
 216 and, in some cases, it took several days before the street could be reopened. For that reason, we started  
 217 to detect and map all landslides caused by the earthquake. In addition, during the field visits in August  
 218 2021, just after the main shock, our teams could confirm that this earthquake had triggered more  
 219 extensive slope failures (covering wider surface areas) than the previous M=7.0 event in January 2010.  
 220 After these visits we started to detect and map all landslides caused by the earthquake.

221

222 3.1.2 Regional mapping of landslides using remote imagery of August – November 2021

223 Mapping of earthquake-induced landslides is often done from pre- and post-event optical and radar

224 satellite imagery; both can be publicly accessible. Optical imagery (that was used for this study) includes,

225 amongst others, like Sentinel-2 (Tanyas et al., 2022) or Landsat-7 and -8 data, with resolutions starting

226 from 10 m, or commercial higher resolution data, that which is often made publicly available for

227 disaster response, through Google Earth, with resolutions of down to 0.5 m e.g. (Harp et al., 2016; Kargel

228 et al., 2016; Wartman et al., 2013). Sometimes mapping is also supported by (pre-event) digital elevation

229 data (Gorum et al., 2011; Kargel et al., 2016) or even by field or helicopter reconnaissance. Landslides

230 are mapped at different levels of spatial discretization, e.g. as landslide initiation points (Gorum et al.,

231 2011), centroid points (Wartman et al., 2013), or landslide polygons (Tanyas et al., 2022), and with a

232 varying degree of detail, e.g. regarding the minimum mapped landslide size or the identification of

233 landslide types. The quality and accuracy of the inventories depend typically on the resolution of the

234 satellite data, cloud cover, and the availability of suitable pre-event data for a clear identification of co-

235 seismic landslides. A recent review of earthquake-induced landslide inventories was presented by Tanyas

236 et al. (2017).

237 In our case, medium-resolution imagery available from the Copernicus Open-Access Hub was used for

238 the landslide mapping over the whole potentially affected area: Sentinel-2, with 10-m spatial resolution

239 bands B2 (490 nm), B3 (560 nm), B4 (665 nm) and B8 (842 nm) collected for eight different dates, every

240 five to six days, between August 14, 2021 (the first one was available about two hours after the main

241 shock), and the end of September 2021 (an example of a Sentinel 2 image view of this period is shown

242 in the annex, in Fig. A2a, presenting a view of the zone located in the map in Fig. 2). Analyzing all

243 images was necessary due to the extensive (but spatially variable) cloud cover present on each image.

244 Considering that only this medium-resolution imagery was freely available in the beginning, the authors

245 are aware that the landslides could not be mapped with the highest precision, and that not all smaller

246 landslides could be identified (especially those smaller than 2000 m<sup>2</sup>, corresponding roughly to 4 by 5

247 pixels on a Sentinel-2 image). However, during the following months, also higher resolution (0.5-1 m)

248 imagery became available on Google Earth Pro® (GEP) for about 50% of the potentially affected

249 region (before December 2021). For these areas, the initial landslide outlines could be refined, and also

250 smaller slope failures could be mapped; an example of the ‘resolution’ effect on landslide mapping is

251 shown in the annex, by Fig. A2, comparing the aforementioned Sentinel 2 image (black-white, projected  
252 on the topography in GEPro) with a higher resolution image of the same landslide zone that became  
253 available on GEPro in September 2021. On the basis of such comparisons between higher and lower  
254 resolution imagery, we could see that most larger landslides are actually composed of multiple initially  
255 smaller and narrower slides and flows, which had coalesced to form a larger coherent mass. ~~(while a lse~~  
256 ~~e~~Even on the higher resolution imagery no clear separation could be outlined within the ~~ise~~ landslide  
257 areas); ~~actuallyindeed~~, the refinement could only help identify distinct sources of those larger mass  
258 movements, but the outline of the main sliding mass often remained the same. Furthermore, for most  
259 landslide zones, no clear distinction could be made between landslide scarp and deposits, as it can often  
260 be observed for such kind of disrupted mass movements.

261

262 32.1.3 Regional mapping of landslides using remote imagery of November 2014 – August 2021, with  
263 focus on pre-seismic changes that occurred in October 2016

264 For the entire area, also a comparison with pre-event imagery was completed to be sure that only ‘co-  
265 seismic’ (or nearly co-seismic – see explanation below) slope failures had been mapped; this check was  
266 especially necessary for the identification of the smaller co-seismic landslides. Therefore, the impacted  
267 region was screened by using high resolution (0.5-1 m) imagery available on GEPro for the period  
268 between 2014 and August 2021. A pre-earthquake image (of November 28, 2014) of the same landslide-  
269 impacted area is shown in Fig. 3a, highlighting the contrast between the vegetated slopes present in the  
270 target region and the extensive denudation that occurred during the earthquake of August 2021 (see  
271 images shown in Fig. 3d, identical to the one shown in the annex in Fig. A2a). However, we could also  
272 observe by comparing multiple images available for the pre-event period that some denudation had  
273 already appeared for smaller zones before 2021. Zones marked by narrow debris slides and flows could  
274 be outlined especially on images available for the time just after October 10, 2016. Fig. 3b presents an  
275 image of October 12, 2016 that shows the ‘freshest’ type of denudation since 2014 (see yellow polygons  
276 outlining such denudation zones), some of which disappeared after a few years (see Fig. 2c), due to  
277 revegetation of the slopes (rapid revegetation can be observed as the whole area is located in tropical  
278 regions). This image and others available for the same period were added to GEPro after Hurricane  
279 Matthew had impacted, in early October 2016, the same area as the one hit by the 2021 earthquake. The

280 consequences of this 'double' impact on the target region will be analyzed in the sections 3 and 4 on the  
281 basis of precipitation distribution maps.

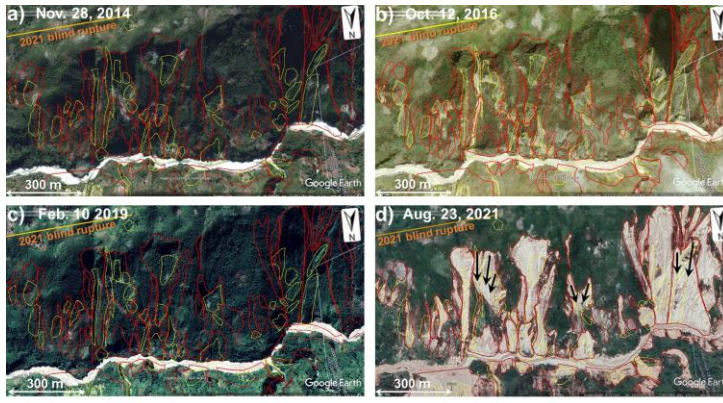
282 Actually, Haiti is quite often (at least once per year) crossed by hurricanes or severe tropical storms, some  
283 of which can trigger slope failures over wide areas. One such tropical storm that later developed into the  
284 hurricane called Grace had also crossed southern Haiti, just two to three days after the August 14, 2021,  
285 main shock. We introduce this fact here in the methodological part as it had two consequences for the  
286 landslide mapping: ~~First~~, right after the earthquake wide areas were covered by clouds during several  
287 days (some higher mountain parts even for weeks); thus, multiple satellite images of different dates (both  
288 Sentinel-2 and higher resolution imagery on GEPro) had to be inspected to map landslides over the whole  
289 area. Second, we had to consider that Grace might also have induced slope failures and that landslides  
290 mapped by using post-hurricane imagery were not all seismically triggered, or were at least enlarged by  
291 the effects of Grace. Therefore, by comparing the post-seismic, August 14, Sentinel-2 image (collected  
292 before the Hurricane Grace event) with the one of August 29, 2021 (post-seismic and post-hurricane),  
293 we checked if additional or enlarged slope failures had appeared on the latter. An example of such a  
294 comparison is presented in Fig. A3, where red arrows point to zones marked by larger slope failures on  
295 the Sentinel-2 image of August 29, 2021, ~~which~~ The latter were thus most likely reactivated by rainfall  
296 during the Grace climatic event (disregarding here the possible additional influence of aftershocks  
297 occurring at the same time in the region that could not be checked due to missing new high-resolution  
298 imagery after each event; it should also be noted that none of the aftershocks had a magnitude. Mw. larger  
299 than 6). Unfortunately, due to the extensive cloud cover in mid-August 2021, such a comparison could  
300 only be completed for about 10% of the seismically impacted area. For those cloud-free zones, we  
301 estimate that Grace had mainly induced a widening of the initially seismically triggered slope failures,  
302 but the importance of this reactivation process cannot be quantified due to the extensive cloud cover and  
303 related shadow effects on the surface. However, we could at least see that no new landslides had been  
304 triggered within the earthquake-affected cloud-free zones. Effects of Hurricane Grace outside the region  
305 marked by stronger shaking have not been studied – this would require a completely new mapping  
306 approach.–

307

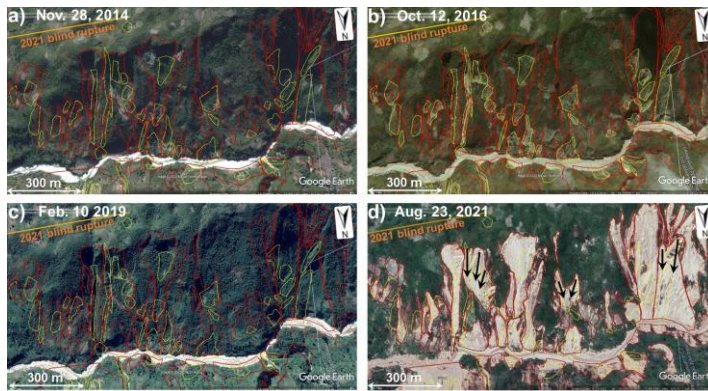
308

309

310



311



312 Figure 3: Evolution of landslides within the zone marked in Fig. 2 between November 2014 (view a), after  
313 Hurricane Matthew (Oct. 2016, b), a view of the area of Feb. 2019 (c) and of Oct. 2021, about two months of  
314 the earthquake (an image of August exists, but it is partly cloudy). Landslides that occurred during or directly  
315 after the Hurricane Matthew event are outlined in yellow and those that were triggered by the August 14,  
316 2021, earthquake are shown by dark red polygons; see also black arrows marking the coalescence of landslides  
317 with distinct sources (only for three examples shown). All views on © Google Earth Pro.

318

319 **3.2.2** Landslide distribution statistics, climatic context and a first size-frequency analysis

320 In sub-section 4.3.2, observed total landslide numbers and surface areas as well as other parameters  
 321 characterizing the statistics of the two inventories, the new one presented here for 2021 and the one for  
 322 2010 by Harp et al. (2016), are compared with ‘predicted’ ones. The latter numbers are computed  
 323 according to prediction laws proposed by Havenith et al. (2016) and Malamud et al. (2004). To estimate  
 324 the total number ( $N_{LT}$ , see Eq. 1) of landslides triggered by a specific earthquake, Havenith et al. (2016)  
 325 recommend to take into consideration the shaking intensity factor, ( $I$ , based on the Arias Intensity, see  
 326 Arias (1970), and thus on the earthquake magnitude,  $M$ ; see Eq. 6b in the next sub-section), the fault  
 327 factor  $F$  (depending on the type,  $FT$ , and size of the fault rupture, considering also the influence of a  
 328 possible surface rupture), the topographic energy ( $TE$ , using mainly as parameter the maximum altitude  
 329 difference in the affected region), the climatic background ( $CB$ ) conditions, and the lithological factor  
 330 ( $LF$ , depending on the presence of soft soils for instance). Related factor values used for the calculations  
 331 are compared with estimated minimum and maximum values in Table 2, in the following section.

$$332 \quad N_{LT} = 1000 \times I \times F \times TE \times CB \times LF, \quad (1)$$

333 Compared with the prediction of the total number of landslides triggered by a specific earthquake  
 334 proposed by Havenith et al. (2016), the one recommended by Malamud et al. (2004) is much simpler (Eq.  
 335 2) and only based on the earthquake magnitude,  $M$ .

$$336 \quad N_{LT} = 10^{(1.29M - 5.65)}, \quad (2)$$

337 For the calculation of the total area potentially affected by landslides ( $A_{Lext}$ , area within the maximum  
 338 extent of landslide occurrence, equivalent to the area of distribution defined by Marc et al., 2017, and  
 339 Tanyas and Lombardo, 2019) Havenith et al. (2016) propose the following Eq. (3), which also directly  
 340 considers the earthquake magnitude,  $M$ , and the hypocentral Depth,  $D$ :

$$341 \quad A_{Lext} = I \times FT \times TE \times CB \times LF \times M \times D^2, \quad (3)$$

342 As Havenith et al. (2016), Keefer and Wilson (1989) also propose an equation to estimate the total area  
 343 potentially affected by landslides during one earthquake event. Their estimate of  $A_{Lext}$  is purely based on  
 344 the earthquake magnitude, similar to Eq. (2) proposed by Malamud et al. (2004) to estimate  $N_{LT}$ :

$$345 \quad A_{Lext} = 10^{(M - 3.46)}, \quad (4)$$

346 Malamud et al. (2004) do not propose any formula to estimate the total area potentially affected by



347 landslides during an earthquake event as Havenith et al. (2016) (see Eq. 3), but recommend the following  
348 prediction law (Eq. 5) to estimate the total area effectively covered by co-seismic landslides,  $A_{LT}$ , based  
349 on the observed or predicted (using Eq. 2, or any other related prediction law, such as the one in Eq. 1)  
350 total number of landslides:

$$351 \quad A_{LT} = 0.00307 N_{LT}, \quad (5)$$

352 All the previous equations were used to compute the respective values presented in Table 1 in sub-section  
353 [4.3.2](#).

354 Size-frequency relations were computed for the 7091 landslide outlines in terms of frequency-density  
355 function (FDF) on the basis of the measured surface areas,  $f(A_L)$ . The same statistics were also computed  
356 for the 23,567 landslides mapped by Harp et al. (2016). Therefore, we used the method introduced by  
357 Malamud et al. (2004) for surface areas (Eq. 6):

$$358 \quad f(A_L) = \frac{\delta N_L}{\delta A_L} \quad (6)$$

359 where  $\delta N_L$  is the number of landslides with areas between  $A_L$  and  $A_L + \delta A_L$  (representing the difference  
360 between two landslide surface area classes). Surface areas were calculated in  $\text{km}^2$ . Related distributions  
361 computed, respectively, for each landslide catalogue (for the 2010 one by Harp et al., 2016; and for the  
362 new 2021 inventory) are then compared with theoretical frequency-density distributions, as proposed by  
363 Malamud et al. (2004). The latter are based on the three-parameter inverse-gamma probability  
364 distribution (see equation 3 in Malamud et al., 2004) that is multiplied by the total number of landslides  
365 of simulated events (100, 1000, etc.). In this regard, it should be noted that the original technique  
366 proposed by Malamud et al. (2004) to complete the size-frequency statistics is based on the probability-  
367 density values, corresponding to the frequency-density values divided by the total number of mapped  
368 landslides,  $N_{LT}$  (which can be fit by the aforementioned three-parameter inverse-gamma probability  
369 distribution). However, as indicated above, due to the limited amount of high-resolution imagery  
370 available for the area potentially affected by seismic shaking in August 2021, not all small landslides  
371 could be mapped; therefore, the total number of landslides seismically triggered in August,  $N_{LT}$ , is likely  
372 to be higher than 7091 (even if the potential ‘hurricane-effect’ is removed, as explained below), and the  
373 probability-density function cannot be correctly computed. For such cases, Malamud et al. (2004)



374 recommend the computation of the frequency-density function to assess the completeness of the  
375 inventory by comparison with the aforementioned predefined theoretical frequency-density functions, as  
376 it will be shown for the 2010 and 2021 inventories in the following results section.

377 To provide information about the climatic context covering different periods of time, we used the Global  
378 Precipitation Measurement Mission (GPM, by NASA) data obtained via the  
379 <https://giovanni.gsfc.nasa.gov/> website, corresponding to the merged satellite-gauge monthly  
380 precipitation estimate (in mm), assessed with a resolution of 0.1°. Related maps were extracted for all  
381 months between August 2000 and July 2021, and also for the specific months of October 2016 and August  
382 2021, as well as for all October months between 2000 and 2020. Note, we also extracted maps for shorter  
383 periods around the climatic events of Matthew in 2016 and Grace in 2021, but those did not provide any  
384 additional information. Additionally, we tried to support these merged satellite - rain gauge estimates by  
385 additional ground measurement data. However, the *Centre National de l'Information Géo-Spatiale*,  
386 *CNIGS*, of Haiti, informed us that such data would not be available; therefore, we can only rely on these  
387 regional estimates.

### 388 **3.2.3 Mapping of seismic landslide triggering factors**

389 The aforementioned climatic data are supposed to help us better understand the pre-conditioning of slope  
390 stability in the target area and thus will also be used below for the interpretation of the landslide  
391 distribution statistics. However, it is obvious that for such an event the main trigger factors are still related  
392 to earthquake shaking; those have to be assessed to understand why extensive slope instability could be  
393 observed in one zone and only isolated minor failures occurred in another one. Such an analysis is  
394 completed both for the 2010 and 2021 events, by computing the Arias Intensity distribution maps (for  
395 2010, comparing the results with the landslide distribution as observed by Harp et al., 2016).

396 The Arias Intensity,  $I_a$ , can be considered as a quantitative measure of the degree of shaking (in m/s) on  
397 the surface. With respect to any other intensity characterization (including the one based on surveys) it  
398 has the advantage to be more objective and comparable for different earthquakes (according to Harp and  
399 Wilson, 1995). Wilson and Keefer (1985) were the first to try to correlate seismically triggered landslide  
400 distributions with this intensity measure. They also defined the following empirical attenuation  
401 relationship (Eq. 7a) in terms of magnitude ( $M$ ) and hypocentral distance ( $R$ ):

402  $\log(I_a) = -4.1 + M - 2 \log(R) + 0.5P$  , (7a)

403 where P considers a possible deviation from the main law (P=0 stands for the average value).

404 Afterwards, Keefer and Wilson (1989) have reviewed the application of this formula and defined a new  
405 one (Eq. 7b), for magnitudes greater than 7:

406  $\log(I_a) = -2.35 + 0.75M - 2 \log(R)$  , (7b)

407 We applied the latter equation as both the 2010 and 2021 can be considered as  $M \geq 7$  events. The R-  
408 value represents the hypocentral distance map, here computed by using as source zone the blind fault  
409 rupture segments of the 2010 and 2021 events (with 0 km epicentral distance and 10 km hypocentral  
410 depth along the respective segment; information extracted from [earthquake.usgs.gov](http://earthquake.usgs.gov)).

411 All equations introduced above have been applied to obtain the computation results presented below, in  
412 the sub-sections 4.3.2 and 4.3.4.

### 413 **3.4 Results: landslide inventory statistics and analysis of trigger conditions**

414 This section first summarizes a series of landslide type and general distribution characteristics. Second,  
415 landslide inventory and size-frequency statistics are presented and supported by an inventory  
416 completeness analysis. Third, a study of possible climatic slope failure preconditioning and post-seismic  
417 landslide surface changes is presented, which also compares landslide distributions with monthly  
418 precipitation maps (using output maps of the Global Precipitation Measurement Mission, GPM, produced  
419 by the NASA, for different periods, according to Acker and Leptough, 2007). Fourth, the landslide  
420 occurrence observed in 2010 and in 2021 is compared with respective shaking intensity prediction maps.

#### 421 **4.3.1 Landslide type and distribution characteristics**

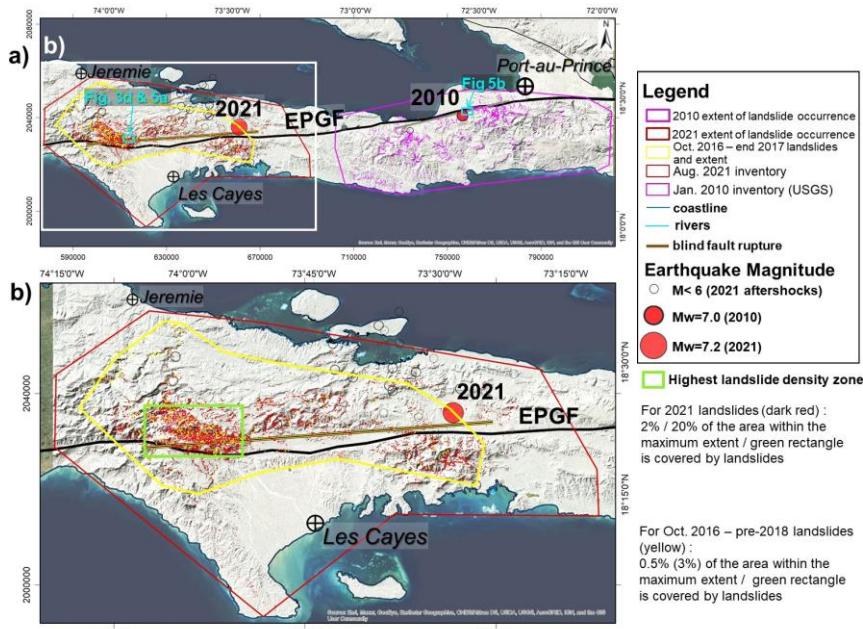
422 Before analyzing specific statistical values of the two landslide inventories, the one compiled by Harp et  
423 al. (2016) for the 2010 event and ours completed after the August 2021 earthquake, we first have a look  
424 at the general respective spatial landslide distributions and provide basic information on the type of the  
425 mapped landslides.

426 The map presented in Fig. 4a shows that the global extent of landslides triggered in 2010 (pink outlines  
427 within the pink maximum extent polygon) and in 2021 (dark red outlines within the dark red maximum

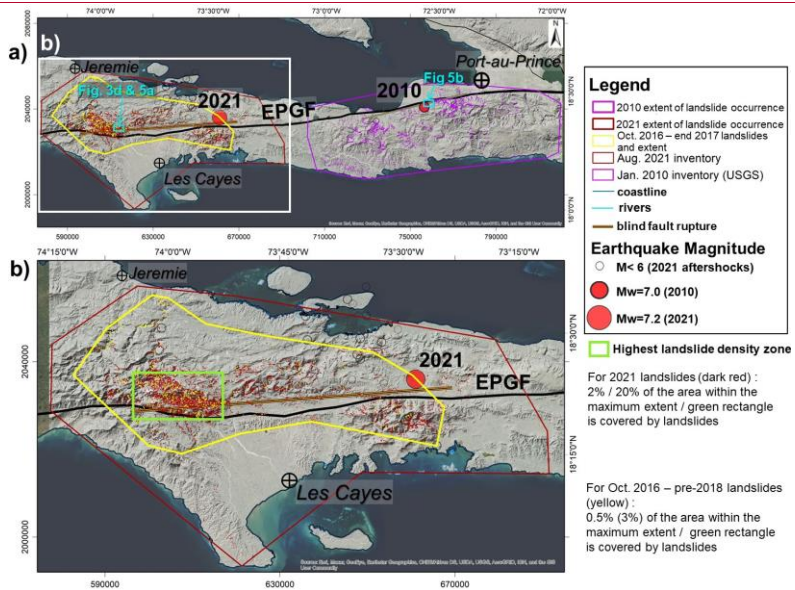
428 extent polygon) is quite similar (exact values are presented in Table 1). This map also shows the location of  
429 the main shock and aftershocks (empty circles, from earthquake.usgs.gov) and the outline of the (roughly 80 km  
430 long) blind fault rupture (extracted from USGS page:  
431 <https://earthquake.usgs.gov/earthquakes/eventpage/us6000f65h/finite-fault>). Outlines of mapping zones shown  
432 presented in Fig. 5 are shown by light blue rectangles. A major difference between the two landslide  
433 distributions can mainly be observed with respect to the location of the EPGF zone. While most  
434 landslides occurred in the south of the fault zone in 2010, a relatively symmetric distribution of landslides  
435 with respect to the location of the EPGF zone can be observed for the 2021 event. This is mainly due to  
436 the fact that the fault segment that ruptured near EPGF in 2010 is located close to the coast (actually just  
437 in the south of the coast, as can be seen in the map in Fig. 4a), and thus only limited onshore surface  
438 areas could be affected by landslides in the north of the EPGF zone in 2010, while However, the location  
439 of the fault segment that ruptured in 2021 is more central within the southwestern peninsula of Haiti (see  
440 focus on this region in Fig. 4b).

441 Another important observation is that there seems to be a gap between the zone affected by landslides in  
442 2010 and the one affected in 2021. This means that, according to our present observations, the 2021  
443 earthquake did not reactivate landslides triggered in 2010 – due to the large distance (> 60 km) between  
444 the fault ruptures. However, it should be noted that this check could only be completed so far with the  
445 10-m resolution Sentinel-2 imagery. Now, we cannot exclude that very small landslides (that we cannot  
446 identify on Sentinel 2 imagery) triggered in 2010 had been reactivated in 2021.

Formatted: Centered



447



448

449 Figure 4: a) Study region with areas affected, respectively, by the two Mw >= 7 events. Individual landslides  
450 triggered in 2010 (Harp et al., 2016, inventory) and our landslides mapped for the 2021 earthquake and

451 **October 2016 hurricane events are shown, respectively, as pink, dark red and yellow polygons. The maximum**  
452 **extent of landslides triggered in 2010, in 2021 and 2016 is outlined, respectively, by the large pink, dark red,**  
453 **and yellow polygons. b) Focus on the region hit by the August 2021 earthquake, with 7091 landslide locations.**  
454 **Map background by © ESRI.**  
455

456 An important consequence of the specific location of the ruptured fault segments is that a few dozens of  
457 landslides with a surface area larger than 2000 m<sup>2</sup> had occurred along the shore in 2010, where the two  
458 or three largest ones (likely including an important submarine part) had massively impacted the ocean  
459 and, thus, had produced up to 3 m-high tsunami waves (see Olson et al., 2011; Poupardin et al., 2020;  
460 Fritz et al., 2013; Sassa and Takagawa, 2018). ~~while~~However, there is not a single report of a major  
461 coastal landslide for the 2021 event – as the fault rupture occurred at a distance of minimum 10 km away  
462 from the nearest shoreline. Instead, a wider onshore area was exposed to high intensity earthquake  
463 shaking during the 2021 event. The related impact will be analyzed below on the basis of the statistical  
464 values presented in Table 1.

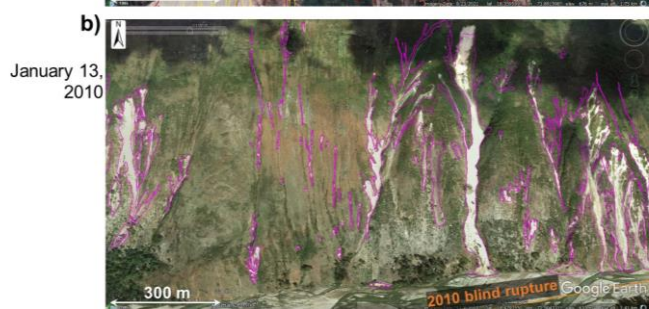
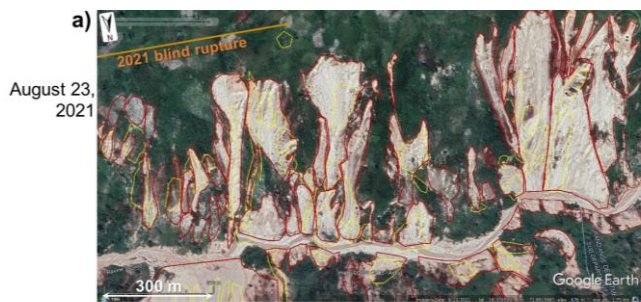
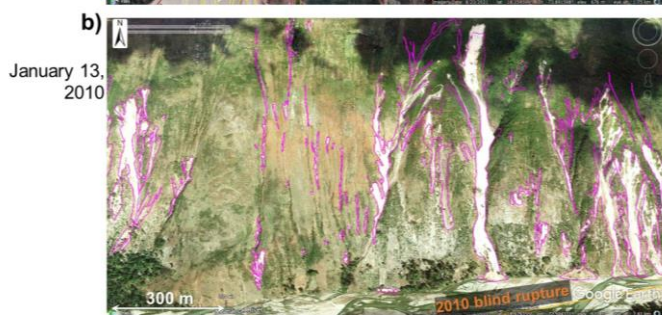
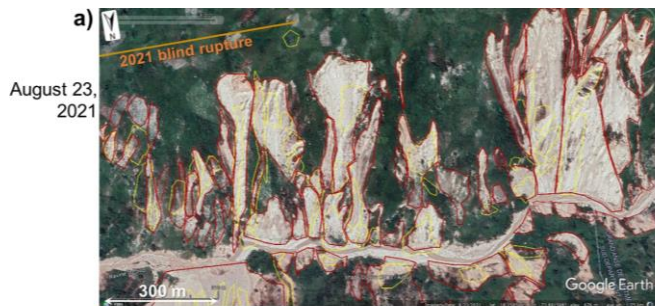
465 Concerning the types of landslides triggered by the 2021 earthquake, we can say that by far most of them  
466 can be classified as debris slides or flows (see examples in the GEPPro view presented in Fig. 5a) and as  
467 medium-size (most with a volume of less than 20,000 m<sup>3</sup>) rockfalls (as shown above in Fig. 2). Thus, we  
468 estimate that at least 95% of all landslides mapped are relatively shallow (with a depth of less than 10  
469 m). Actually, not a single large massive landslide (> 10<sup>7</sup> m<sup>3</sup>) could be identified. A similar observation  
470 was made by Harp et al. (2016) for the landslides triggered in 2010 (see view in Fig. 5b). However, when  
471 comparing individual landslides induced in 2021 with those triggered in 2010, the latter are almost  
472 systematically narrower than those of 2021 (compare the very narrow slides and flows in Fig. 5b with  
473 the typically wider ones in Fig. 5a), while located in similar geological (limestone) and topographic  
474 (hilly-mountainous) environments. Actually, in the so-called *Ravine du Sud* (Gorge of the South), part of  
475 which is shown above in Fig. 3 (and in the annex, in Figs. A2 and A3), numerous very extensive slope  
476 failures (but still relatively shallow) could be observed; most of them formed by coalescent neighboring  
477 debris slides. Thus, entire slope units (delimited by upper and lateral slope crests and the valley bottom)  
478 finally collapsed as one single mass movement. Such kind of extensive slope failures occurred far less

479 frequently in 2010 – at least onshore, while at least a few aforementioned coastal and mostly submarine  
480 landslides must have been quite massive as their impact had triggered tsunami waves, as indicated above.  
481 This assumption cannot be further verified as no higher resolution marine floor surface data are available.  
482 However, we are aware that a full mapping of submarine or mixed subaerial-submarine slope failures  
483 would be necessary to better understand the landslide distribution characteristics, especially for the 2010  
484 event, as further discussed below.

485 The fact that no really massive landslides had occurred (onshore), both in 2010 and 2021, also explains  
486 why only a few longer lasting landslide dams had formed on the rivers. We could identify only about 100  
487 minor dams (with a volume of less than 50,000 m<sup>3</sup>, according to our estimate, based on the maximum  
488 surface area value of about 5000 m<sup>2</sup> measured for the largest observed dam and a related maximum  
489 possible thickness of 15 m, compared with the local morphological setting) after the August 2021 main  
490 shock, most of which had disappeared before the end of October 2021; and, only a few dozens of them  
491 were impounding temporary lakes. In this regard it should be noted that [Zhao et al. \(2022\) do not make](#)  
492 [any reference to landslide dams formed in 2021 while](#) Martinez et al. (2021), ~~who had also mapped~~  
493 ~~landslides triggered by the 2021 Nippes earthquake (4893, according to their open file report)~~, have  
494 outlined almost 300 (at least partial) landslide dams after the event. However, the [latter](#) also indicate  
495 that most of them failed a few days after formation; still, at the time of publication of their open file  
496 report in December 2021, they consider 35 of the remaining dams as potentially hazardous. Here, we  
497 will not further analyze this aspect as any related hazard assessment would require a site-specific  
498 approach that is not targeted by this first study completed at regional scale.

499





502 Figure 5: a) GEPro view (© Google Earth Pro) of landslides triggered by the August 2021 earthquake. b)

503 GEPro view (© Google Earth Pro) of landslides induced by the January 2010 main shock (with landslide

504 outlines by Harp et al., 2016).

505

506 While debris slides are the predominant type of 2021 slope failures in the central mountain ranges,  
507 widespread soil slides (but of smaller volume, typically of less than 10,000 m<sup>3</sup>) had occurred along the  
508 hills (with an absolute crest altitude of less than 400 m, and a relative height of less than 200 m with  
509 respect to the nearby valley bottom) of the peninsula located in the southwest of Les Cayes (southern  
510 part of map in Fig. 4b). As the slopes are very gentle, often seem to be less than 5°, it could be that those  
511 failures, many of which affected agricultural areas (marked by brownish disrupted fields), are related to  
512 liquefaction phenomena. However, also this observation has to be reexamined, by ground-control and  
513 site-specific studies, as the remote analysis based on 1-m resolution imagery does not allow us to fully  
514 confirm this interpretation. —

## 515 **4.2 Landslide inventory and size-frequency statistics**

### 516 **4.2.1 Landslide inventory statistics**

517 Table 1 presents an overview of general landslide inventory statistics, for both the 2010 and 2021 events.  
518 The numbers in the first row show that apparently fewer landslides have been triggered in August 2021  
519 (considering also the numbers of 4893 landslides published in the open file report by Martinez et al.,  
520 2021, and of 8444 landslides mapped by Zhao et al., 2022) than in January 2010. At least two inventories,  
521 the one by Harp et al. (2016) and the one of Xu et al. (2014), include far more landslide outlines (23,567  
522 for the first, 30,828 for the second) than our catalogue for 2021 (7091). Only the inventory by Gorum et  
523 al. (2013) that was the first one to be completed for the 2010 event contains fewer data (4490 points –  
524 not polygons - marking the landslide location). However, paradoxically, a much wider surface area is  
525 covered by the apparently fewer 2021 landslides (a total area of 84 km<sup>2</sup>, see row 3 in Table 1, also to be  
526 compared with a smaller total area of 2021 landslides indicated by Zhao et al., 2022, of 45.6 km<sup>2</sup>) than  
527 by the more numerous 2010 landslides (sum of surface areas of about 25 km<sup>2</sup>, calculated for the Harp et  
528 al., 2016, inventory). This discrepancy will be discussed below, considering the fact that 2021 landslides  
529 could only be mapped from higher resolution imagery for about half of the potentially affected area (in  
530 the eastern part). For the western zone, only Sentinel-2 images were available until the end of 2021.

Formatted: Superscript



531 Those 10-m resolution images typically do not allow for the (complete) mapping of landslides smaller  
532 than 2000 – 3000 m<sup>2</sup>. Therefore, we focus only general landslide inventory statistics, first, by comparing  
533 the observed landslide numbers with those predicted by Havenith et al. (2016) and Malamud et al. (2014),  
534 respectively, for the two earthquakes – always keeping in mind that the 2021 inventory is not complete  
535 for landslides smaller than about 3000 m<sup>2</sup> (this value will also be analyzed below on the basis of the size-  
536 frequency relationship). As introduced above (see Eq. 1), according to Havenith et al. (2016), this number  
537 depends on the seismic intensity (I, using as input the I<sub>a</sub> value computed for the respective earthquake  
538 magnitude), the fault factor (type, size and possible surface rupture), the topographic energy (maximum  
539 difference of altitudes in the affected area), the climatic background (in this case marked by tropical wet  
540 climate), and the lithological factor (here using an average type, for rocks in general). For the precise  
541 classification of the different factors, the reader is referred to Table 1 in Havenith et al. (2016). Here, we  
542 used the values presented below in Table 2 (considering both events in 2010 and 2021), which indicate  
543 the following:

544 1) the shaking intensity values, I=0.74, in 2010, and I=1 in 2021 are characteristic for the respective  
545 magnitudes (note, this factor can reach a value of up to 3.5 in the case of high-magnitude earthquakes,  
546 with  $M_w > 8$ );

547 2) the fault factor, F=2.25, can be considered as similar in both cases, marked by an oblique slip that  
548 occurred along a fault segment with a length of 50-100 km, with no clear surface rupture (note, F can  
549 reach a value of up to 6 in the case of a surface rupture of an activated reverse fault segment with a length  
550 of more than 300 km, such as observed for the Wenchuan earthquake in 2008);

551 3) the topographic energy value, TE=2, in both cases characterizes a surface morphology marked by local  
552 altitude changes of more than 500 m within a hilly region (only smaller mountains, with an altitude of  
553 less than 2500 m can be found in the regions affected by the 2010 and 2021 events; note, Havenith et al.,  
554 2016, selected a value 4 to mark the high steep slopes in the Longmenshan Mountains affected by the  
555 Wenchuan earthquake in 2008);

556 4) the climatic background factor, CB=1.5 marks relatively wet conditions for the 2021 event while CB=1  
557 indicates average conditions for the 2010 event (the higher value chosen for 2021 considers some  
558 preconditioning of slope instability by Hurricane Matthew, as explained in the next section; note,  
559 Havenith et al., 2016, selected a value CB=2 for the very wet conditions that can be found in the

560 Longmenshan Mountains affected by the Wenchuan earthquake, characterized by yearly precipitation  
561 values of more than 3000 mm – while the target areas in Haiti are marked by values of about 2000 mm);  
562 5) the lithological factor,  $LF=2$ , indicates that both weathered rocks and soft soils can be found in the  
563 affected area (note, Havenith et al., 2016, selected a maximum value,  $LF=4$ , for the Haiyuan-Gansu-  
564 Ningxia earthquake event, China, in 1920, as it affected an area that is almost entirely covered by Loess  
565 deposits, which are highly susceptible to slope failure).

566 When these different factor values are combined according to Eq. (1) presented above, the total numbers  
567 of landslides,  $N_{LT}$ , predicted for the 2010 and 2021 events are, respectively, 6694 and 13,476. These  
568 values can be compared with the numbers predicted by the simple equation (Eq. 2), proposed by  
569 Malamud et al. (2004), using only the earthquake magnitude as input: 2399 for the 2010 event and 4345  
570 for the 2021 event. The latter prediction seems to clearly underestimate the observed numbers of  
571 triggered landslides, while those predicted by using Eq. (1) by Havenith et al. (2016) provide intermediate  
572 values: larger than the number observed by Gorum et al. (2013) but smaller than the numbers observed  
573 by Harp et al. (2016) and by Xu et al. (2014). The two predictions (Eq. 1 and 2) were also applied to the  
574 2021 event; the first one producing a higher  $N_{LT}$  (=13,476) than the observed value, the second one  
575 producing a lower value (=4345).

576 As shown on the maps in Fig. 5, also the total area within the maximum extent of landslide occurrence,  
577  $A_{L,ext}$ , was outlined and then measured for the 2010 and 2021 events. Actually, related areas are relatively  
578 similar: 4400 km<sup>2</sup> for 2021 and 4100 km<sup>2</sup> for 2010. It should be noted that Zhao et al. (2022) identified  
579 all 2021 landslides within a smaller extent area of 2700 km<sup>2</sup>. This can partly be explained by the fact that  
580 they did not map any landslides in the southern zone (marked by the presence of the smaller soil slides).  
581 All these~~These~~ values can be compared in Table 1 with the predictions by Havenith et al. (2016) and by  
582 Keefer and Wilson (1989), corresponding, respectively, to 3124 and 3467 km<sup>2</sup>, for the 2010 event, and  
583 to 6470 and 5495 km<sup>2</sup>, for the 2021 event. In this case, the very simple equation proposed by Keefer and  
584 Wilson (1989) provides an estimate of  $A_{L,ext}$  that is closer to the observed values than the one produced  
585 by the more complex relationship proposed by Havenith et al. (2016).

586 The third row of Table 1 compares the total observed slope areas affected by landslides,  $A_{LT}$ ,  
587 corresponding, respectively, to a value of 24.86 km<sup>2</sup> for the 2010 event and of 84.38 km<sup>2</sup> for the 2021  
588 event (the latter value being significantly smaller for Zhao et al., 2022, close to 45 km<sup>2</sup>), with the values

Formatted: Superscript

589 predicted by Eq. (5) by Malamud et al. (2004) for each event. For 2010, we applied this relationship to  
590 the three observed values indicated in the first row and by using the  $N_{LT}$ , predicted respectively by  
591 Havenith et al. (2016) and Malamud et al. (2004). Among all total landslide surface area values predicted  
592 for the 2010 event, it can be seen that the one based on the Havenith et al. (2016)  $N_{LT}$  estimate produces  
593 the best fit ( $=20.55 \text{ km}^2$ ) when compared with the observed value of  $24.86 \text{ km}^2$ . For 2021, the respective  
594 predictions all underestimate the observed total landslide surface area value,  $A_{LT}$ , by a factor of at least  
595 two, even when the highest  $N_{LT}$  estimate (using Eq. 1) by Havenith et al. (2016) is used. Using the  
596 preceding information, it is also useful to compare the density values (here, expressed in %) of landslide  
597 areas within the maximum extent surface area, which correspond to 0.5% and 2%, respectively for the  
598 2010 and 2021 events. Within the green rectangle (zone with highest landslide density) shown in Fig. 4  
599 above, even 20% of all the area is covered by landslides. Possible explanations for the much larger total  
600 area (and the higher density) of landslides triggered in 2021 compared with 2010 will be provided in the  
601 discussion.

602 The fourth and fifth rows show that the smallest landslide mapped by Harp et al. (2016) has a surface  
603 area of  $0.5 \text{ m}^2$  and their inventory contains 6587 landslide polygons smaller than  $100 \text{ m}^2$  while our  
604 inventory for 2021 only includes one landslide with a surface area smaller than this value. This  
605 comparison also confirms that our inventory is likely to be incomplete for such small landslides, as there  
606 is no physical reason why there would be much fewer smaller landslides triggered in 2021 than in 2010.  
607 On the other hand, the largest landslide mapped for the 2021 event ( $>400,000 \text{ m}^2$ ) has almost twice the  
608 size of the largest one that occurred in 2010, when actually only 2 landslides larger than  $100,000 \text{ m}^2$  had  
609 been triggered; in 2021, we could outline more than 100 landslides larger than this value. And, for these  
610 larger landslides we can be sure that we mapped them all and outlined them correctly, without  
611 amalgamating distinct slope failures.

612 Finally, Table 1 provides information about the distribution of the 2010 and 2021 landslides with respect  
613 to the blind fault rupture projected on the surface (near the EPGF outline). As already introduced above,  
614 a much larger number of landslides occurred in the north of the latter in 2021 ( $=4678$ , [~66% of all](#)  
615 [landslides](#)) compared to 2010 ( $=2548$ , at least for onshore slope failures); [for 2021, Zhao et al. \(2022\)](#)  
616 [even mapped 89.4% of all landslides \(7548 landslides as indicated in Table 1\) in the north of the activated](#)  
617 [fault. This higher proportion of landslides in the north of the fault compared to ours can also partly be](#)

618 explained by the fact that Zhao et al. (2022) did not map any distant soil slides in the south of the fault  
 619 rupture. Consequently, more landslides occurred in 2010 in the south of the respective blind fault rupture.  
 620 As the total number of mapped landslides is much larger for the 2010 event (which also means that only  
 621 the relative proportions should really be considered), the difference between those numbers is very high:  
 622 21,019 occurred in the south of the fault rupture in 2010 (about 90% of all landslides) and only 2420 in  
 623 the south of the respective fault rupture in 2021 (about 35%). However, when the total surface area  
 624 affected by landslides is considered, the 2021 event affected more zones both in the south and the north  
 625 of the fault rupture than the 2010 event, while Still, the distribution of landslides for each event with  
 626 respect to the fault rupture remains the same also when considering the affected surface areas: they are  
 627 much larger in the south of the fault rupture for the 2010 event but larger in the north for the 2021 event.  
 628 The main explanation for this difference has already been provided above: the fault segment that ruptured  
 629 in 2010 is located close to the coast, with limited onshore surface areas being exposed to landslide activity  
 630 in the north of the respective fault rupture, while the location of the fault rupture in 2021 is more central  
 631 with respect to the shorelines of the southwestern peninsula of Haiti.  
 632

633 **Table 1: 2010 and 2021 landslide inventory characteristics – where not specified for the 2010 event, using the**  
 634 **Harp et al. (2016) inventory. The largest values for each specific observation/estimate (if more than 1 indicated)**  
 635 **are bold.**

Landslide inventory parameters/predictions	2010, Mw=7.0	2021, Mw=7.2
Observed number of landslides, $N_{LT}$	>4490 <sup>a</sup> / 23,567 <sup>b</sup> / <b>30,828<sup>c</sup></b>	<b>7091</b> /4893 <sup>d</sup> / <b>8444<sup>e</sup></b>
Havenith et al. (2016) $N_{LT}$ prediction 1	6694	13,476
Malamud et al. (2004) $N_{LT}$ prediction 2	2399	4345
Area of region potentially affected by landslides, $A_{Lext}$ (km <sup>2</sup> )	4100	4400/ <b>2700<sup>e</sup></b>
Havenith et al. (2016) $A_{Lext}$ prediction 1	3124	6470
Keefer and Wilson (1989) $A_{Lext}$ prediction 2	3467	5495
Total surface area of landslides, $A_{LT2}$ (km <sup>2</sup> )	24.86	84.38/ <b>45.6<sup>e</sup></b>
Malamud et al. (2004) $A_{LT}$ prediction :		
for the observed $N_{LT}$	13.8 <sup>a</sup> / 72.3 <sup>b</sup> / <b>94.6<sup>c</sup></b>	21.8
for the $N_{LT}$ prediction 1	20.55	41.4

Formatted: Superscript

Formatted: Superscript

for the N <sub>LT</sub> prediction 2	7.36	13.3
Smallest landslide (m <sup>2</sup> )	0.5	75
Number of landslides smaller than 100 m <sup>2</sup>	6587	1
Largest landslide (m <sup>2</sup> )	234,370	409,479/ <sup>310,000</sup>
Number of landslides larger than 100,000 m <sup>2</sup>	2	103
Total number of landslides in the north (N) / south (S) of the fault rupture	N= 2548 S= <b>21,019</b>	N= <del>4678</del> / <sup>7548</sup> S= 2420/ <sup>896</sup>
Total surface area of landslides in the N / S of the fault rupture (km <sup>2</sup> )	N= 2.45 S= <b>22.41</b>	N= <b>58.31</b> S= 26.07

Formatted: Superscript

Formatted: Font: Not Bold

Formatted: Font: Not Bold

Formatted: Superscript

Formatted: Superscript

636 <sup>a</sup> Number of landslides observed for the 2010 event by Gorum et al. (2013), <sup>b</sup> by Harp et al. (2016), <sup>c</sup> by  
637 Xu et al. (2014), and, for the 2021 event, <sup>d</sup> by Martinez et al. (2021) and <sup>e</sup> by Zhao et al. (2022).

Formatted: Superscript

638

639 In addition to the numbers shown in Table 1 and explained above, we also provide two values for the  
640 smaller landslide inventory compiled for the period between October 10, 2016 and the end of 2017. For  
641 this period, 625 landslide zones have been outlined (see yellow polygons shown on the views and map  
642 in Figs. 3 and 4), covering a total surface area of 9.5 km<sup>2</sup> (located within an area of maximum extent of  
643 these landslides of 1770 km<sup>2</sup> as outlined in yellow, above in Fig. 4) This also means that about 0.5% of  
644 the area within the maximum extent was covered by landslides. Highest concentration of landslides can  
645 be observed within the green rectangle shown in Fig. 4, where 3% of the total area is covered by  
646 landslides. However, we must indicate that these values represent approximations as only 50% of the  
647 potentially affected area is covered by cloud-free imagery on GEPro for this period, most of which  
648 actually covers the short period between October 10 and 28, 2016 (just after Hurricane Matthew event).  
649 Post-2017 imagery was not used as we could observe that many landslides identified shortly after Oct.  
650 10, 2016, had already ‘disappeared’ in 2018-2020 due to revegetation of the affected area (see, above,  
651 the comparison between GEPro views of October 2016 and February 2020 in Fig. 3).

652 **Table 2: Factors contributing to the total number and surface area of landslides triggered by the 2010 and the**  
653 **2021 earthquakes, according to the prediction proposed by Havenith et al. (2016). The minimum and**  
654 **maximum values proposed by Havenith et al. (2016) are also indicated, the latter with information on the**  
655 **event – region, to which this maximum factor value was attributed.**

Haiti Events/ Factors	Shaking Intensity, I	Fault Factor, F (type, FT)	Topographic Energy, TE	Climatic Background, CB	Lithological Factor, LF	Hypocentral Depth, D (km)
2010	0.74	2.25(1.5)	2	1.5	2	10
2021	1	2.25(1.5)	2	1	2	10
min. values	0.1	0.75	1	0.5	1	10
max. values (event - region)	3.4 (Chile, 1960)	6 (Wenchuan, 2008)	4 (Wenchuan, 2008)	2 (Wenchuan, 2008)	4 (Haiyuan-Gansu- Ningxia, 1920)	226 (Hindu Kush, 2002)

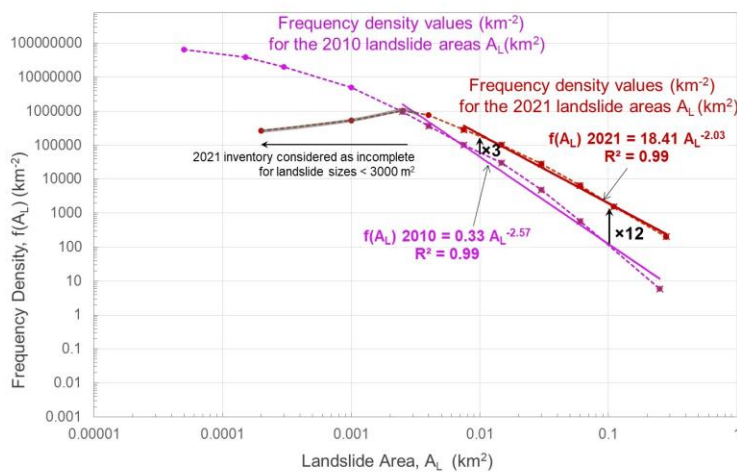
656

657 [4.2.2](#) Landslide size-frequency statistics

658 We also computed frequency-density values for various landslide surface area classes as shown on the  
659 graph in Fig. 6. There are two important parameters to be analyzed for the observed frequency-density  
660 distributions, according to Malamud et al. (2004), among others: the first part is represented by the  
661 power-law decay (see also introduction in Stark and Hovius, 2001) that appears as a linear decay in the  
662 log-log graph below; the second part is the so-called ‘rollover’, which can be observed for a landside  
663 surface area where the exponentially decreasing number of larger landslides turns into a decrease of the  
664 number of smaller landslides. Here, we will only focus on the power-law decay that can be observed for  
665 the larger landslides, for which we consider both, the 2010 and the 2021, inventories as complete. Fig. 6  
666 shows that such a power-law decay can be observed for 2010 landslides larger than 2000 m<sup>2</sup> and for 2021  
667 landslides larger than about 4000 m<sup>2</sup>. This comparison confirms the likely incompleteness of the 2021  
668 inventory, even for landslides smaller than 4000 m<sup>2</sup>. The rollover part will not be analyzed here as it  
669 occurs for smaller landslides, well below this limit of completeness of our 2021 inventory (referring to  
670 estimates by Malamud et al., 2004).

671 For the larger landslides, the comparison between frequency density outputs of the 2010 and 2021  
672 landslide inventories presented in Fig. 6 first shows that related values are higher for the latter catalogue.  
673 Actually, related frequency density values are three times larger for the landslide size class of 10,000 m<sup>2</sup>  
674 and even twelve times for the one of 100,000 m<sup>2</sup>. And, for those larger landslide classes, the absolute  
675 value of the power-law decay is slightly higher (-2.57, for the pink line fitting the 2010 data) for the 2010  
676 inventory than for the 2021 one (-2.03, for the red line fitting the 2021 data – to be compared with the  
677 equivalent value of -2.47 determined by the Zhao et al., 2022, for their inventory). Thus, the relative  
678 smaller decay exponent observed for the 2021 landslide inventory explains why related frequency density

679 values are increasingly (i.e. for larger landslide sizes) higher compared with the 2010 values observed  
 680 for the same landslide size classes. These different size-frequency characteristics of the 2010 and 2021  
 681 landslides inventories will shortly be discussed below (considering the constraint of inventory  
 682 completeness for both events), but the most important information to be retained at this level is that for  
 683 all landslide classes larger than 4000 m<sup>2</sup> more landslides have been observed in 2021 than in 2010.



684  
 685 **Figure 6: Frequency density graphs developed for the 2010 (in pink, by Harp et al., 2016) and the new 2021**  
 686 **landslide inventories (in dark red), with related power-law decays outlined.**

687 **3.4.3 Climatic (pre- and post-seismic) conditioning of slope instability**

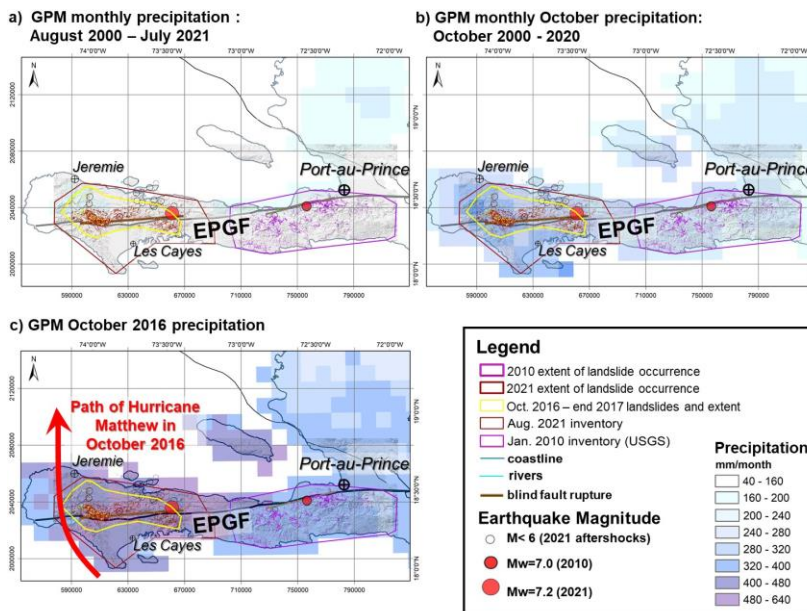
688 The climatic influence on landslide occurrence (in 2021) has been introduced above, by considering the  
 689 possible impacts of hurricanes on slope failure occurrence, marked both by preconditioning of slope  
 690 instability and by post-seismic intensification. We first start analyzing the last effect, by considering the  
 691 potential impact of Hurricane Grace on post-seismic landslide intensification, on August 16-17, 2021  
 692 (when it had crossed the target region and was actually classified as tropical depression at that stage). A  
 693 possible effect of related rainfalls on landslide occurrence has already been highlighted, for instance, on  
 694 the AGU Landslide blog (by Petley, D., 2021, on [blogs.agu.org/landslideblog](https://blogs.agu.org/landslideblog)). This effect could be  
 695 confirmed when we compared Sentinel-2 imagery collected right after the earthquake (2h after the main

696 shock) with images remotely sensed after August 17, 2021. As indicated above and shown in Fig. 4, an  
697 intensification of denudation could indeed be observed after the tropical storm Grace event. However,  
698 one important limitation has to be highlighted: this comparison could only be completed for about 10%  
699 of the area potentially hit both by the earthquake and by Grace, due to the intense cloud cover present in  
700 the target region during that period. Furthermore, another effect could have contributed to slope failure  
701 intensification after the main shock on August 14, the one related to the aftershocks (see empty circles  
702 shown in all maps above), ~~but~~ However, analyzing this effect would require a refinement of the satellite  
703 image analysis both in space and time, which is hardly possible considering the extensive cloud cover  
704 present in the target area when all those seismic shocks occurred. Here, we will focus on the possible  
705 climatic influence, which can better be outlined when comparing the landslide distribution with actual  
706 precipitation maps. Therefore, we used the aforementioned Global Precipitation Measurement Mission  
707 (GPM) data. Fig. 7 presents the three following types of GPM maps: average monthly precipitation maps  
708 for the whole period of 2000 – July 2021, for all months of October between 2000-2020, and for October  
709 2016, when Hurricane Matthew had crossed the island. Additionally, we compare in Fig. A4 the first and  
710 third map with the precipitation map produced for August 2021, when Hurricane Grace had affected the  
711 target area.

712 While comparing the average monthly precipitation rates between 2000 and 2021 (Fig. 7a) with the one  
713 of October 2016 (Fig. 7c) we can see that, for the latter month, a peak of intensity of 626 mm can be  
714 observed for the area between Gran Rivière De Nappe and Petite-Rivière-de-Nippes, situated  
715 immediately in the north of the epicentral area of the 2021 main shock. Actually, the whole area  
716 potentially affected by the August 2021 earthquake had been exposed to clearly higher precipitation rates  
717 of more than 400 mm in October 2016, while, according to the GPM, average precipitation recorded in  
718 October between 2000 and 2020 varies typically between 200 and 320 mm (as shown by the map, in Fig.  
719 8b). For October 2016, those values were also the highest ones compared with the rest of the country and  
720 are also larger than those obtained for August 2021 (max. 320mm) for the target zone, when Hurricane  
721 Grace had crossed this region. ~~This~~ clearly indicates that the precipitation values must be related to a  
722 specific (and even exceptional) climatic event, which can easily be identified as Hurricane Matthew that  
723 had crossed the western peninsula (including the region hit later by the August 2021 earthquake) on  
724 October 4-5, 2016. And, precisely for this region that had been exposed to abnormal precipitation rates



725 in October 2016, we could outline 625 landslides triggered after the Hurricane Matthew event, and before  
 726 the end of 2017 (yellow polygons shown above in the maps in Figs 1, 2, 3 and 4 and below in Fig. 7).  
 727 ~~And~~ Additionally, most of these October 2016 – end of 2017 landslide zones (at least 90% of them) are  
 728 located within those mapped for the August 2021 seismic event (which are still marked by a much higher  
 729 level of denudation compared to the October 2016 activation). In the discussion, we will analyze how  
 730 such Hurricane Matthew might have preconditioned slope instability in the region hit by the August 14,  
 731 2021, earthquake. We will also consider a general influence of tropical storms on the wide distribution  
 732 of the landslides triggered in 2010 (and also for those triggered in 2021, in addition to the Hurricane  
 733 Matthew effect).



734  
 735 **Figure 7: Monthly © Global Precipitation Measurement Mission (NASA) maps (0.1° resolution, values in**  
 736 **mm/month) for southwestern Haiti, (a) for all months between August 2000 and July 2021, (b) for the month**  
 737 **of October between 2000 and 2020, and (c) for October 2016 (marked by the Hurricane Matthew event).**

738 By comparing equivalent data (not shown here) of the merged satellite-gauge precipitation estimate for  
 739 August 2021 with the monthly precipitation map averaged for all months of the previous 20 years, we

740 can clearly see that August 2021 was indeed marked by a higher precipitation rate, which is most likely  
741 related to the Grace event. However, the most intense precipitation did not affect the region hit by the  
742 2021 earthquake but the eastern part of the peninsula, roughly covering the same region as the one  
743 affected by the 2010 event (note, we did not check any landslide reactivation after Grace for that area).  
744 The region hit by the 2021 earthquake was not affected by much higher monthly precipitation rates than  
745 usual: for the central seismically affected zone, in the north of Les Cayes, about 240-280 mm had been  
746 recorded in August 2021, against a monthly average of 200 mm. Thus, just by considering these data,  
747 one would not expect an important climatic contribution to slope failure occurrence in the region affected  
748 by the 2021 earthquake. Still, an influence could be observed and this is likely to be related to the  
749 concentration of most of the 'monthly precipitation' of August 2021 within the two days (Aug. 16 and  
750 17) of the Grace tropical storm event, just two days after the 2021 main shock. As indicated above, we  
751 estimate that related precipitation has resulted in an increase of landslide surface areas of about 10-15%.  
752 Due to the limited extent of zones where this check can be made (only considering the cloud-free areas  
753 on the Sentinel-2 image of August 14, 2021), it was decided to map all areas covered by landslides after  
754 August 14, 2021, also those which are likely to have been (re)activated by rainfall. ~~The~~ The total effect of  
755 ~~which~~ ~~the latter~~ can barely be controlled and quantified outside the 10% of cloud-free zones visible on  
756 the image collected right after the main shock. The only 'correction' that can be made is to reduce the  
757 total surface area mapped as landslides by those 10-15% to estimate the one that was actually affected  
758 by co-seismic slope failures: thus, instead of considering the value of 84 km<sup>2</sup>, it is possible that co-seismic  
759 landslides covered a total surface area of 'only' 75-78 km<sup>2</sup> – which is still three times more than the total  
760 surface area covered by 2010 co-seismic landslides (close to 25 km<sup>2</sup>).

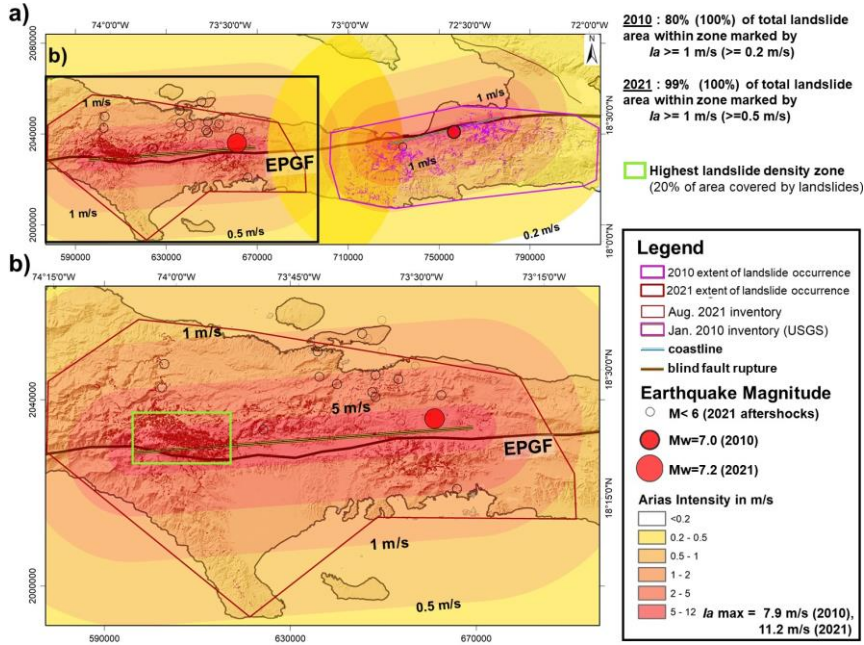
761

#### 762 **4.3.4 Shaking intensity maps**

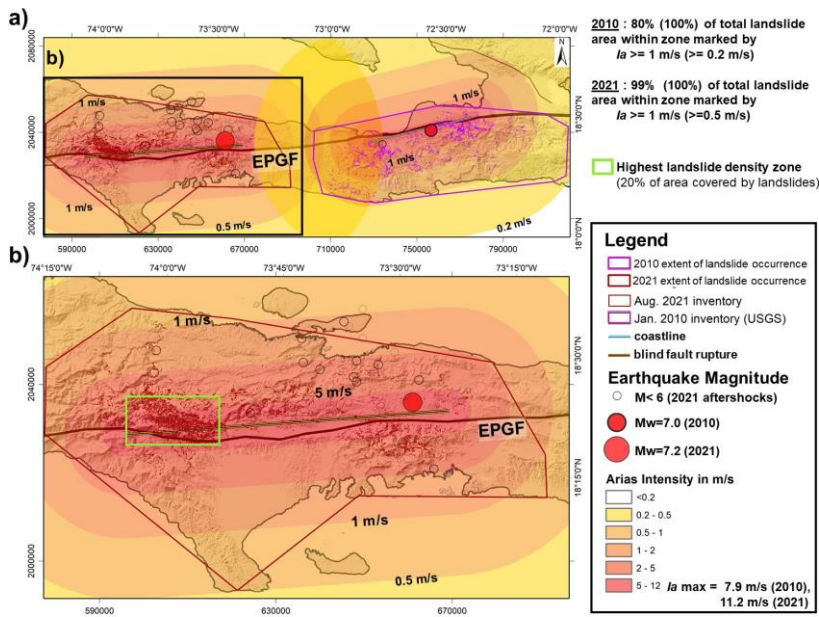
763 Above, we first analyzed the possible climatic influence on seismically induced slope failures as it could  
764 affect the landslide distribution and thus has to be taken into consideration when assessing and  
765 interpreting the seismic effect on landslide occurrence. The latter will only be analyzed here at regional  
766 scale. Therefore, we compare the landslide distributions observed for the 2010 and 2021 events with the  
767 respective estimated Arias Intensity (I<sub>a</sub>) attenuation maps, computed by applying Eq. (7b) introduced

768 above, as recommended by Wilson and Keefer (1985) and also by later studies (e.g., Harp and Wilson,  
769 1995, among many others). The map in Fig. 8a presents the 2010 and 2021 mainshock Ia attenuation  
770 values, with a maximum shaking intensity of 11.2 m/s computed for the 2021 event and 7.9 m/s for 2010  
771 (respective maps are partly overlapping in the central region, but not summed up, keeping the individual  
772 values). This map shows that all 2010 and 2021 landslides are included within a zone marked by an Ia  
773 threshold of 0.2 m/s (close to the one proposed by Keefer and Wilson, 1989, for disrupted slides and  
774 falls). Actually, for 2021, 99% of the total landslide surface areas are even located within a zone marked  
775 by Ia values larger than 1 m/s; however, only 80% of the total surface areas of the 2010 landslides are  
776 included within the respective  $I_a \geq 1$  m/s zone. Thus, the latter mass movements appear as more  
777 ‘dispersed’ with respect to the estimated seismic intensity attenuation than the 2021 ones. The [2021](#)  
778 [landslides](#) are [indeed](#) most concentrated, as indicated above, within the green rectangle (see Fig. 8b,  
779 marked by Ia values of 4-11 m/s) with an area of 200 km<sup>2</sup> that contains 40 km<sup>2</sup> of landslide-covered  
780 zones (=20% of total area).

781 Notwithstanding the relative dispersion of 2010 landslides, and the overlap of Ia values larger than 0.2  
782 m/s in the central zone between the two blind fault ruptures of 2010 and 2021, not a single landslide of  
783 2010 seems to have been reactivated in 2021. This observation raises the question if the central ‘landslide  
784 gap’ is due to an overestimation of the Ia values in this central zone (as this zone is marked by Ia values  
785 above the aforementioned minimum threshold of 0.2 m/s, for both events, and thus should have been  
786 affected by landslides both in 2010 and 2021, according to the shaking intensity prediction parameter),  
787 or if this zone is simply less susceptible to (seismic) slope failures.



788



789

790 Figure 8: a) Arias Intensity ( $I_a$ ) attenuation maps computed (by using Eq. 7b, by Keefer and Wilson, 1989)

791 **for the 2010 and 2021 main shocks in Haiti; see also indication of % of total surface area of landslides observed**  
792 **for different Ia thresholds. b) Focus on the respective map computed for the 2021 event.**

793

794 To answer this and other related questions, a full landslide susceptibility analysis has been completed  
795 and will be presented in another paper. Here, only the possible links between landslide distribution the  
796 aforementioned seismotectonic and climatic factors will be discussed.

## 797 **4.5 Discussion**

### 798 **5.4.1 Discussion about landslide distribution characteristics**

799 From the comparison of the two landslide catalogues (2010 and 2021), we could first infer that apparently  
800 not a single landslide triggered in August 2021 occurred within the zone previously impacted by the 2010  
801 event. There is a gap of about 10 km between the westernmost 2010 and the easternmost 2021 landslide  
802 (see gap between the general outlines of the maximum extent of landslides triggered in 2010 and in 2021  
803 shown on the map in Fig. 4a). Thus, we assume that there was no obvious preconditioning of landslide  
804 generation in 2021 by the 2010 event, while landslide studies completed in other parts of the World (e.g.,  
805 by Parker et al., 2015, for events in New Zealand) could outline an influence of previous earthquakes on  
806 landslide occurrence during later events. The absence of this influence by the 2010 earthquake is  
807 probably due to the long distance (the ‘gap’) of about 60 km between the fault segments that ruptured in  
808 2010 and in 2021. However, by citing Saint Fleur et al. (2020), Stein et al. (2021) hint at an older event,  
809 of 1770, with an assumed magnitude of 7.5 and an epicenter located precisely in the gap between the  
810 2010 and 2021 blind fault ruptures, which could also have affected the region hit by the 2021 earthquake.  
811 At present, we cannot exclude that this older event had preconditioned some slopes (by soil weakening,  
812 rock fracturing) affected by some larger landslides in 2021; however, very shallow slope failures initiated  
813 in 1770 are unlikely to have stayed in place over such a long period of more than 250 years, as they  
814 would have been ‘washed’ away by the next tropical rains.

815 Second, none of the two earthquakes triggered very massive landslides, such as deep-seated rockslides  
816 with a volume of more than  $10 \cdot 10^6 \text{ m}^3$  (while extensive areas are covered by layered and weathered

817 limestone that could also produce massive slope failures; but this aspect will not be further discussed  
818 here as the related geological influence on landslide occurrence will be analyzed in the landslide  
819 susceptibility paper presently under preparation). Such massive failures have been observed after many  
820 M7+ events in other mountainous regions of the world: see Fan et al. (2018) for the 2008 Mw=7.9  
821 earthquake in China, or Havenith et al. (2015) for a series of M>7 events that hit Central Asian mountain  
822 regions during the last 120 years. This is partly due to the fact that the regions hit by the two earthquakes  
823 in Haiti are represented by mountains of limited elevation changes, typically less than 1000 m – while,  
824 for instance, the Longmenshan Mountains hit by the 2008 Wenchuan earthquake, present elevation  
825 changes of up to 3000 m over relatively short (<6 km) distances (Fan et al., 2018). This fact, combined  
826 with the higher magnitude of the Wenchuan earthquake (Mw=7.9), could partly explain the much larger  
827 number of massive rockslides triggered by the latter event in China. However, we have also to consider  
828 some counterexamples of regions marked by mountainous relief that did not produce any very massive  
829 rockslides during high-magnitude earthquakes (just like the 2010 and 2021 Haiti events), such as the part  
830 of the Himalayas hit in 2015 by the Gorkha earthquake (see Lacroix, 2016). Thus, this problem related  
831 to the more or less likely occurrence of massive rockslides in regions hit by high-magnitude earthquakes  
832 is relatively complex, and cannot purely be approached by spatial analysis, as the one presented here.  
833 **M**ore extensive numerical simulations would actually be necessary (but are definitely not the target of  
834 our studies in Haiti) to assess the potential of seismically induced rockslides, such as those presented in  
835 Gischig et al. (2015) or Lemaire et al. (2021).

836 Third, considering the values presented in Table 1, we still have to explain why the total surface area  
837 covered by landslides in 2021 is much larger than the one covered by the 2010 landslides. We estimate  
838 that this fact is likely to be related to (a combination of some of) the four following points: a) the first  
839 likely physical reason for the larger area hit by mass movements in 2021 is the higher triggering  
840 earthquake magnitude of the last event (this effect is also analyzed by comparing the influence of shaking  
841 intensity on landslide distribution); b) another physical reason could be the possibly higher susceptibility  
842 to mass movements of the western part of the peninsula hit by the 2021 event, compared to the eastern  
843 part (this factor has to be analyzed on the basis of landslide susceptibility maps, considering also the  
844 geological influence, which have been computed and will be presented in a follow-up paper); c) a third  
845 reason for the larger area affected by landslides in 2021 could be related to the aforementioned ‘hurricane’

846 effects that will be further discussed below; d) and fourth, the more central location of the fault segment  
847 activated in 2021 with respect to the coasts of the peninsula certainly also explains parts of the larger  
848 total surface areas of (subaerial) slope failures triggered during the last event within the wider onshore  
849 hanging wall part, as already introduced above.

850 In this regard, we also highlighted the fact that the 2010 event triggered most landslides in the south of  
851 the activated fault segment, while in August 2021 about 2/3 of all landslides were triggered in the north  
852 of it. Considering the oblique slip character along the fault ruptures of 2010 and 2021 dipping to the  
853 north, the hanging wall is located on the northside of the blind fault rupture projected on the surface -  
854 (according to the fault mechanism provided by the USGS Earthquake Hazard Program page,  
855 [earthquake.usgs.gov](https://earthquake.usgs.gov)). In this regard, the Wenchuan earthquake has clearly marked the effect of the  
856 hanging wall on the landslide distribution: about 90 % of all landslides were triggered on top of the  
857 reverse fault dipping towards the west-northwest, only a minor portion occurred on the more 'stable' foot  
858 wall (Gorum et al., 2011; Fan et al., 2018). The 'hanging wall effect' on landslide triggering can be  
859 explained by stronger upward oriented shaking that contributes to a higher surface acceleration and more  
860 intense slope failures; additionally, all (or most of the) aftershocks occurred within the hanging wall,  
861 increasing the seismic shaking intensity cumulated over the active seismic period in the related surface  
862 area, which could have contributed to prolonged landslide activity as well (to be added to the climatic  
863 effect introduced above and discussed below). This effect may thus also be at the origin of the more  
864 widespread landslide occurrence in the north of the 2021 blind fault rupture. The reduced number of  
865 'subaerial' landslides induced on the hanging wall side of the 2010 fault rupture can be explained by the  
866 relative proximity of the respective fault rupture to the coast in the north and the absence of high and  
867 steep slopes (onshore) on this side. Actually, a few known massive landslides occurred near the coast,  
868 but are mostly located on submarine slopes in the 2010 hanging wall zone. Three of them reportedly also  
869 caused tsunami waves (see Olson et al., 2011, among others) – a phenomenon that was not observed for  
870 the 2021 event, as the coasts are located farther away from the seismic source zone.

#### 871 **5.4.2 Discussion about landslide size-frequency characteristics**

872 Above, we clearly outlined the incompleteness of our 2021 inventory, for landslides smaller than about  
873 3000 m<sup>2</sup>; thus, it is likely that thousands of smaller landslides could not be mapped from the medium-

874 resolution Sentinel-2 imagery (10 m) and the higher resolution imagery (0.5 – 1 m) available on GEPro  
875 for 50% of the target area before the end of 2021. To refine our landslide mapping in future, higher  
876 resolution imagery must be used for the whole area affected by the 2021 event, and automatic landslide  
877 identification techniques shall be applied by combining image analysis and machine learning as proposed  
878 by Amatya et al. (2021). Actually, the ‘manual’ mapping applied now would take too much time to outline  
879 the many thousands of very small landslides that have not been identified so far. Those would contribute  
880 to the increase of the weight of the smaller landslides in the 2021 inventory, especially of those smaller  
881 than 3000 m<sup>2</sup>. ~~It can be assumed that Zhao et al. (2022) have identified a larger number of smaller~~  
882 ~~landslides or have mapped separate landslides where we had considered them as merged larger mass~~  
883 ~~movements, as they obtained a larger absolute value of the decay exponent (=2.47, compared to ours,~~  
884 ~~being 2.03). In addition, the total area affected by landslides mapped by Zhao et al. (2022) is clearly~~  
885 ~~smaller than ours. From the combination of both observations, we may conclude the following: either we~~  
886 ~~have over-mapped landslide areas or, by splitting coalescent mass movements, Zhao et al. (2022) have~~  
887 ~~under-mapped failed slopes.– Providing an answer to this question would require a more detailed~~  
888 ~~analysis of both inventories, which is not possible here. For our inventory we may just say that Theits~~  
889 ~~likely incompleteness of the inventory notably~~ limits its use for size-frequency analyses. ~~However, above~~  
890 ~~we still presented~~ By comparing related statistics ~~and compared them~~ with those made for the 2010  
891 landslide inventory, ~~to point out the clearly higher numbers of~~ we can just say that the last event has  
892 ~~triggered numerous~~ larger landslides ~~triggered by the last event, compared with the one in~~ than the one  
893 ~~in~~ 2010 (based on ‘landslide size’ classes, for which the 2021 inventory can be considered as complete).  
894 Actually, landslides triggered in 2010 mainly consisted of narrow slides and flows in weathered limestone  
895 rocks, while the 2021 earthquake also induced landslide processes over wider slope areas – as clearly  
896 shown by the 2021 and 2010 landslide zone views presented in Fig. 5; in the *Ravine du Sud*, even entire  
897 slope units had failed in August 2021 (but the failed parts were typically not very thick, less than 10 m).

#### 898 **5.4.3 Discussion about climatic pre-conditioning effects**

899 We estimate that the different climatic conditions observed before the respective events may partly  
900 explain the more widespread occurrence of larger landslides related to the 2021 event. In this regard we  
901 indicated that the climatic contribution to landslide activity in 2021 might be twofold: first, some post-



902 seismic intensification of slope failures could be observed after the tropical storm Grace event that had  
903 crossed the earthquake region on August 16-17, two days after the main shock. However, related effects  
904 cannot really be quantified as only 10% of the total surface area potentially affected by the earthquake  
905 appeared as cloud-free on imagery available right after the August 14 main shock and before August 16  
906 (Grace event). For those limited areas, we estimate that storm Grace caused a widening of about 10-15%  
907 of all slope failures with respect to the purely earthquake-induced landslide activation. Second, by  
908 comparing the 2016-2017 landslide distribution with the one observed after August 14, 2021, it can be  
909 seen that most of the October 2016 – end 2017 landslides occurred within the same region as the 2021  
910 ones and most were clearly reactivated by the seismic shaking in August 2021 (while also many of them  
911 had been revegetated in between). Above we could show that Hurricane Matthew had crossed the western  
912 part of the peninsula in October 2016, producing an abnormal amount of precipitation precisely over the  
913 area that was later hit by the earthquake (see GPM maps in Fig. 7), and where also hundreds of landslides  
914 had occurred just after mid-October 2016. Therefore, it is very likely that this climatic event has triggered  
915 many (and probably most) of the 625 mapped pre-seismic (October 2016 - pre-2018) landslides, which  
916 preconditioned slope instability all over the area hit by the 2021 earthquake. Preconditioning of the  
917 August 2021 slope failures could have been related to rock weakening and fracturing, and removal of the  
918 protective vegetation cover during the 2016 Matthew event. Indeed, practically all 625 mapped October  
919 2016 – pre-2018 landslide zones (at least 90% of them – and, considering that only for 50% of the entire  
920 potentially affected area in 2016 landslide could be mapped over cloud-free zones) are located within the  
921 landslide areas mapped for the August 2021 seismic event (which are still marked by a much higher level  
922 of denudation compared to the October 2016 activation). The double hurricane effect (by Matthew in  
923 2016 and by Grace just after the 2021 main shock) observed in the area hit by 2021 earthquake could be  
924 responsible for the proportionally larger size of the 2021 landslides (estimating that the 2016 event, due  
925 to its extreme intensity, made the strongest contribution) compared with the 2010 ones. In addition, we  
926 have to consider that the 2010 earthquake had not been preceded by any particular hurricane event during  
927 the previous ten years, at least not by any storm that had caused abnormal precipitation amounts (similar  
928 to those caused by Hurricane Matthew) within the region hit by the 2010 earthquake.

929 Furthermore, the combined seismic and climatic influence could also explain the very different spatial  
930 landslide distribution characteristics of the 2010 and 2021 catalogues: the relative dispersion of

931 landslides observed after the 2010 event could thus be partly related to the spatially highly variable effect  
932 of tropical storms and hurricanes on landslide activity (acting over a longer period, with an influence that  
933 could last over tens of years), partly overprinting the more concentrated seismic effect (resulting in  
934 clusters of mass movements near the seismic source zone). The same dispersion might also have been  
935 observed for the 2021 event if the central part of the seismically affected area had not been hit by that  
936 major climatic event just five years before – doubling the landslide concentration effect in that area  
937 (specifically for the 2021 event). However, we acknowledge that a quantification of these opposite effects  
938 of climatic events, both on landslide dispersion and on their concentration, requires a more detailed  
939 analysis, ~~also~~ **The latter should also include some studies** focusing on specific sites, by completing  
940 numerical simulations of mass movements affected by variable climatic (modelling changing  
941 groundwater level) and seismic influences (including the effect of rock structures and types of lithologies  
942 and morphologies on shaking polarization and amplification). A related landslide spatial distribution  
943 analysis should then also consider the influence of extensive deforestation on slope destabilization, all  
944 over the country of Haiti. Actually, deforestation is responsible for the decrease of 90% of the primary  
945 forest over the last few tens of years, especially in the southern regions of Haiti where the two earthquake  
946 events had occurred (see Hedges et al., 2018). As mostly shallow landslides occurred in 2010 and 2021,  
947 the effect of deforestation on the destabilization of shallow soils and weathered rock cover must be taken  
948 into consideration for landslide occurrence prediction. Such an extensive study would thus require the  
949 creation of an integrated seismotectonic-morpho-geological-climatic-soil cover model allowing us to  
950 fully understand changing landslide activity in Haiti – which is not the target of the present analysis (but  
951 will be partly approached in the follow-up paper).

#### 952 **4.4 Discussion about the regional seismic shaking influence on landslide distribution**

953 As for the climatic part, here, we only present regional data to outline some general seismic influences  
954 on landslide activity induced by the 2010 and 2021 earthquakes. Related maps (Fig. 8) show that the  
955 aforementioned gap of landslides between the areas affected by the earthquakes in 2010 and 2021 would  
956 indeed be marked both by a lower shaking intensity (but showing values that are still larger than the  
957 threshold Ia values observed elsewhere for landslide occurrence) and lower landslide susceptibility (a  
958 result that still has to be published). In the annex (Fig. A1), we also present the shakemaps produced by

959 the USGS for the two events, but we did not compare landslide distributions with these maps as the latter  
960 do not seem to be coherent with respect to each other, noting that much larger intensities would have  
961 been produced by the lower magnitude event of 2010. Actually, it should be considered that such maps  
962 are also influenced by regional site effects (mostly on flat areas) that are not really relevant for landslide  
963 trigger mechanisms, and are also depending on ground measurements of seismic intensity that had not  
964 been well constrained during the 2010 event due to missing seismic stations in Haiti at that time (a  
965 problem that starts to be solved now).

## 966 ~~65~~ **Conclusions**

967 In this paper we presented a new landslide inventory created for the Mw=7.2 Nippes earthquake that  
968 occurred on August 14, 2021, in Haiti. Related spatial and statistical characteristics have been compared  
969 with those of the landslides mapped by others for the previous, Mw=7.0, January 12 (2010), earthquake  
970 that had occurred along the same fault zone (EPGF zone) but more to the East. Considering a series of  
971 uncertainties affecting the landslide statistics (related to the mapping technique, including the uncertain  
972 number of particularly small landslides triggered in 2021) and the environmental information (including  
973 some general climatic and geological conditions), this comparison allowed us to highlight the following  
974 points: 1) the 2021 earthquake triggered clearly bigger landslides than the one in 2010, and also the sum  
975 of all landslide areas is much larger than the one computed for the 2010 event; 2) a climatic  
976 preconditioning of slope instability could be outlined for the 2021 event, mainly in connection with the  
977 impacts of recent hurricanes in the 2021 affected region, which could also partly explain the more  
978 extensive landslide activity observed in 2021; 3) the 2010 landslides seem to be more dispersed around  
979 the epicentral area than the 2021 slope failures, which could be due to the opposite climatic effect  
980 inducing spatially more variable slope destabilization (also as no particular storm had hit the 2010  
981 affected region just before or after the seismic event, as it was the case in 2021).~~;~~~~†~~This dispersion effect  
982 can also be enhanced by the spatially varying deforestation that is locally very intense in the target areas.  
983 We estimate that this proof of a likely combined seismic and climatic influence on landslide activity  
984 (possibly augmented by morpho-geological and soil cover effects not studied in detail here) opens new  
985 avenues for geohazard research, especially for regions like Haiti that are regularly hit both by severe

986 earthquakes and weather events. We also think that preconditioning of slope failures by multiple events  
987 over longer terms, including by former earthquakes, should be studied more in detail as this  
988 preconditioning could highly contribute to local and regional landslide hazards, both over short and  
989 longer terms. A full analysis of such a scenario would require the development of an integrated  
990 seismotectonic-morpho-geological-climatic-soil (and vegetation) cover model, combining extensive  
991 spatial analyses with detailed numerical simulations, which can only be completed through an extensive  
992 international multi-disciplinary collaboration around this target – which is obviously missing for Haiti.  
993 Assessment of related risk would further require the involvement of experts in social geography and  
994 economy. Also, a closer collaboration between scientists and the population shall be promoted as  
995 recommended by Calais et al. (2022) and von Hillebrandt-Andrade and Vanacore (2022). Only when  
996 these goals are achieved, we could really work on the prevention of at least parts of another future  
997 earthquake disaster in Haiti.

998

#### 999 **Acknowledgments**

1000 This study was partly supported by the ‘Earthquake Hazard and Vulnerability assessment – developing  
1001 innovative solutions for sustainable Risk Reduction and Communication in Haiti’ project funding (2019-  
1002 2024) provided by the Belgian ARES – ACADÉMIE DE RECHERCHE ET D’ENSEIGNEMENT  
1003 SUPÉRIEUR.

1004

1005 **References**

1006  
1007 Acker, G., and Leptoukh, G.: Online Analysis Enhances Use of NASA Earth Science Data, Eos, Trans.  
1008 AGU, 88(2), 14–17, 2007.

1009 [Ali, S. T., Freed, A. M., Calais, E., Manaker, D. M., and McCann, W. R.; Coulomb stress evolution in](#)  
1010 [Northeastern Caribbean over the past 250 years due to coseismic, postseismic and interseismic](#)  
1011 [deformation, Geophys. J. Int., 174\(3\), 904–918, doi.org/10.1111/j.1365-246X.2008.03634.x, 2008.](#)

1012 Amatya, P., Kirschbaum, D., Stanley, T., and Tanyas, H.: Landslide mapping using object-based image  
1013 analysis and open source tools, Eng. Geol., 282, 10 p., doi:10.1016/j.enggeo.2021.106000, 2021.

1014 Arias, A.: A measure of earthquake intensity, In Seismic design for Nuclear Powerplants, R.J. Hansen  
1015 (ed), MIT Press, Cambridge, Massachusetts, 438–483, 1970.

1016 [Bakun, W. H., Flores, C. H., and ten Brink, U. S.; Significant Earthquakes on the Enriquillo Fault System,](#)  
1017 [Hispaniola, 1500–2010: Implications for Seismic Hazard, Bull. Seis. Soc. Am., 102\(1\), 18–30,](#)  
1018 [doi.org/10.1785/0120110077, 2012.](#)

1019 Calais, E., Freed, A., Mattioli, G., Amelung, F., Jónsson, S., Jansma, P., Hong, S. H., Dixon, T., Prépetit,  
1020 C., and Momplaisir, R.: Transpressional rupture of an unmapped fault during the 2010 Haiti  
1021 earthquake, Nature Geoscience, 3(11), 794–799, doi:10.1038/ngeo992, 2010.

1022 Calais, E., Symithe, S., Monfret, T., Delouis, B., Lomax, A., Courboux, F., Ampuero, J.P., Lara, P.E.,  
1023 Bletery, Q., Chèze, J., Peix, F., Deschamps, A., de Lépinay, B., Raimbault, B., Jolivet, R., Paul, S., St  
1024 Fleur, S., Boisson, D., Fukushima, Y., Duputel, Z., Xu, L., and Meng, L.: Citizen seismology helps  
1025 decipher the 2021 Haiti earthquake, Science, 15, 376 (6590), 283-287, doi:10.1126/science.abn1045,  
1026 2022.

1027 [DeMets, C., E.Jansma, P., Mattioli, G. S., Dixon, T. H., Farina, F., Bilham, R., Calais, E., and Mann, P.;](#)  
1028 [GPS geodetic constraints on Caribbean-North America plate motion, Geophys. Res. Lett., 27\(3\), 437-](#)  
1029 [440, doi.org/10.1029/1999GL005436, 2000.](#)

1030 Fan, X., Juang, C.H., Wasowski, J., Huang, R., Xu, Q., Scaringi, G., van Westen, C.J., and Havenith,  
1031 H.B.: What we have learned from the 2008 Wenchuan Earthquake and its aftermath: A decade of research  
1032 and challenges, Eng. Geol., 241, 25–32, doi:10.1016/j.enggeo.2018.05.004, 2018.

Formatted ...

Formatted: Font: Not Bold

Formatted ...

Formatted: Font: Not Bold

Formatted ...

Formatted: Font: Not Bold

Formatted ...

Formatted: Font: Not Bold

Formatted ...

Formatted: Font: Not Bold

Formatted ...

Formatted: Font: Not Bold

Formatted ...

Formatted: Font: Not Bold

Formatted ...

Formatted: Font: Not Bold, English (United States)

Formatted ...

Formatted: Font: Not Bold

Formatted ...

Formatted: Font: Not Bold

Formatted ...

Formatted: Font: Not Bold

Formatted ...

Formatted: Font: Not Bold, Not Italic

Formatted ...

Formatted: Font: Not Bold

Formatted ...

Formatted: Font: Not Bold

Formatted ...

Formatted: Font: Not Bold

Formatted: Font: (Default) Times New Roman, 10 pt

Formatted: Font: (Default) Times New Roman, 10 pt

Formatted: Font: (Default) Times New Roman, 10 pt

Formatted: Font: (Default) Times New Roman, 10 pt

Formatted ...

Formatted: Font: Not Italic

Formatted ...

Formatted: Font: Not Italic

Formatted ...

Formatted: Font: Not Italic

Formatted: Font: (Default) Times New Roman, 10 pt

Formatted: Font: (Default) Times New Roman, 10 pt

Formatted: Font: Not Italic

1033 Frankel, A., Harmsen, S., Mueller, C., Calais, E., and Haase, J.: Seismic hazard maps for Haiti.  
1034 Earthquake Spectra, 27(SUPPL. 1), 23–41, doi:10.1193/1.3631016, 2011.

1035 Fritz, H. M., Hillaire, J. V., Molière, E., Wei, Y., and Mohammed, F.: Twin tsunamis triggered by the 12  
1036 January 2010 Haiti earthquake, Pure and Applied Geophysics, 170(9), 1463–1474, doi:10.1007/S00024-  
1037 012-0479-3, 2013.

1038 Gischig, V., Eberhardt, E., Moore, J., and Hungr, O.: On the seismic response of deep-seated rock slope  
1039 instabilities — insights from numerical modeling. Eng. Geol., 193, 1–18, doi:  
1040 10.1016/j.enggeo.2015.04.003, 2015.

1041 Gorum, T., Fan, X., van Westen, C.J., Huang, R., Xu, Q., Tang, C., and Wang, G.: Distribution pattern  
1042 of earthquake-induced landslides triggered by the 12 May 2008 Wenchuan earthquake, Geomorph.,  
1043 133(3–4), 152–167, doi:10.1016/j.geomorph.2010.12.030, 2011.

1044 Gorum, T., van Westen, C.J., Korup, O., van der Meijde, M., Fan, X., and van der Meer, F.D.: Complex  
1045 rupture mechanism and topography control symmetry of mass - wasting pattern, 2010 Haiti earthquake,  
1046 Geomorph., 184, 127–138, doi:10.1016/j.geomorph.2012.11.027, 2013.

1047 Harp, E.L., and Wilson, R.C.: Shaking intensity thresholds for rock falls and slides: evidence from 1987  
1048 Whittier Narrows and Superstition Hills earthquake strong-motion records, Bull. Seis. Soc. Am., 85,  
1049 1739–1757, 1995.

1050 Harp, E.L., Jibson, R.W., and Schmitt, R.G.: Map of landslides triggered by the January 12, 2010, Haiti  
1051 earthquake: U.S. Geological Survey Scientific Investigations Map 3353, 15 p., 1 sheet, scale 1:150,000.  
1052 doi:10.3133/sim3353, 2016.

1053 Havenith, H.B., Strom, A., Torgoev, I., Torgoev, A., Lamair, L., Ischuk, A., and Abdrakhmatov, K.: Tien  
1054 Shan Geohazards Database: Earthquakes and Landslides, Geomorph., 249, 16–31,  
1055 doi:10.1016/j.geomorph.2015.01.037, 2015.

1056 Havenith, H.B., Torgoev, A., Braun, A., Schlögel, R., and Micu, M.: A new classification of earthquake-  
1057 induced landslide event sizes based on seismotectonic, topographic, climatic and geologic factors,  
1058 Geoenviron. Disasters, 3(6), 2–24, doi:10.1186/s40677-016-0041-1, 2016.

1059 Hedges, S.B., Cohen, W.B., Timyan, J., and Yang, Z.: Haiti's biodiversity threatened by nearly complete  
1060 loss of primary forest, Proc. Nat. Ac. Sc., 115(46), 11850–11855, doi: 10.1073/pnas.1809753115, 2018.

1061 Kargel, J., Leonard, G., Shugar, D., Haritashya, U., Bevington, A., Fielding, E., Fujita, K., Geertsema,  
1062 M., Miles, E., Steiner, J., Anderson, E., Bajracharya, S., Bawden, G., Breashears, D., Byers, A., Collins,  
1063 B., Dhital, M., Donnellan, A., Evans, T., Geai, M., Glasscoe, M., Green, D., Gurung, D., Heijen, R.,  
1064 Hilborn, A., Hudnut, K., Huyck, C., Immerzeel, W., Liming, J., Jibson, R., Kääh, A., Khanal, N.,  
1065 Kirschbaum, D., Kraaijenbrink, P., Lamsal, D., Shiyin, L., Mingyang, L., McKinney, D., Nahirmick, N.,  
1066 Zhuotong, N., Ojha, S., Olsenholler, J., Painter, T., Pleasants, M., Pratima, K., Yuan, Q., Raup, B., Regmi,  
1067 D., Rounce, D., Sakai, A., Donghui, S., Shea, J., Shrestha, A., Shukla, A., Stumm, D., Kooij, M. van der,  
1068 Voss, K., Xin, W., Weihs, B., Wolfe, D., Lizong, W., Xiaojun, Y., Yoder, M., and Young, N.: Geomorphic  
1069 and geologic controls of geohazards induced by Nepal's 2015 Gorkha earthquake, *Science*, 351,  
1070 doi:10.1126/science.aac8353, 2016.

1071 Keefer, D.K., and Wilson, R.C.: Predicting earthquake-induced landslides, with emphasis on arid and  
1072 semi-arid environments, In *Landslides in a Semi-arid environment* (Inland Geological Society, Sadler  
1073 and Morton, eds.), 2, 118–149, 1989.

1074 Lacroix, P.: Landslides triggered by the Gorkha earthquake in the Langtang valley, volumes and initiation  
1075 processes, *Earth Planets Space*, 68(46), 10 p., doi: 10.1186/s40623-016-0423-3, 2016.

1076 Lemaire, E., Mreyen, A.-S., Dufresne, A., and Havenith, H.-B.: Analysis of the influence of structural  
1077 geology on the massive seismic slope failure potential supported by numerical modelling. *Geosciences*,  
1078 10(8), 323, 30 p., doi:10.3390/geosciences10080323, 2020.

1079 Malamud, B. D., Turcotte, D. L., Guzzetti, F., and Reichenbach, P.: Landslide inventories and their  
1080 statistical properties, 29, 687–711, doi:10.1002/esp.1064, 2004.

1081 Marc, O., Meunier, P., and Hovius, N.: Prediction of the area affected by earthquake-induced landsliding  
1082 based on seismological parameters, *Nat. Hazards Earth Sys.*, 17, 1159–1175, doi:10.5194/nhess-17-  
1083 1159-2017, 2017.

1084 Martinez, S.N., Allstadt, K.E., Slaughter, S.L., Schmitt, R., Collins, E., Schaefer, L.N., and Ellison, S.:  
1085 Landslides triggered by the August 14, 2021, magnitude 7.2 Nippes, Haiti, earthquake, U.S. Geological  
1086 Survey Open-File Report 2021–1112, 17 p., doi:10.3133/ofr20211112, 2021.

1087 Okuwaki, R., and Fan, W.: Oblique convergence causes both thrust and strike-slip ruptures during the  
1088 2021 M 7.2 Haiti earthquake, *Geoph. Res. Letters*, 49(2), 12 p., doi:10.1029/2021GL096373, 2022.

1089 Olson, S., Green, R., Lasley, S., Martin, N., Cox, B., Rathje, E., Bachhuber, J., and French, J.:  
1090 Documenting Liquefaction and Lateral Spreading Triggered by the 12 January 2010 Haiti Earthquake,  
1091 Earthquake Spectra, 27, 93–116, doi:10.1193/1.3639270, 2011.

1092 Parker, R.N., Hancox, G.T., Petley, D.N., Massey, C.I., Densmore, A.L., and Rosser, N.J.: Spatial  
1093 distributions of earthquake-induced landslides and hillslope preconditioning in the northwest South  
1094 Island, New Zealand, Earth Surface Dynamics, 3 (4), 501–525, doi:10.5194/esurf-3-501-2015, 2015.

1095 Petley, D.: Landslides from the 14 August 2021 earthquake in Haiti, On  
1096 blogs.agu.org/landslideblog/2021/09/03/landslides-from-the-14-august-2021-earthquake-in-haiti, 2021.

1097 Poupardin, A., Calais, E., Heinrich, P., Hébert, H., Rodriguez, M., Leroy, S., Aochi, H., and Douilly, R.:  
1098 Deep submarine landslide contribution to the 2010 Haiti earthquake tsunami, Nat. Hazards Earth Syst.  
1099 Sci., 20, 2055–2065, doi:10.5194/nhess-20-2055-2020, 2020.

1100 Saint Fleur, N., Klinger, Y., and Feuillet, N.: Detailed map, displacement, paleoseismology, and  
1101 segmentation of the Enriquillo-Plantain Garden Fault in Haiti, Tectonophysics, 778, 25 p.,  
1102 doi:10.1016/j.tecto.2020.228368, 2020.

1103 Sassa, S., and Takagawa, T.: Liquefied gravity flow-induced tsunami: first evidence and comparison  
1104 from the 2018 Indonesia Sulawesi earthquake and tsunami disasters, Landslides, 16, 195–200,  
1105 doi:10.1007/s10346-018-1114-x, 2018.

1106 Stark, C. P., and Hovius, N.: The characterization of landslide size distributions, Geoph. Res. Letters,  
1107 28(6), 1091–1094, doi:10.1029/2000GL008527, 2001.

1108 Stein, R.S., Toda, S., Lin, J., and Sevilgen, V.: Are the 2021 and 2010 Haiti earthquakes part of a  
1109 progressive sequence? Temblor, doi:10.32858/temblor.197, 2021.

1110 Symithe, S. J., Calais, E., Haase, J. S., Freed, A. M., and Douilly, R.: Coseismic Slip Distribution of the  
1111 2010 M 7.0 Haiti Earthquake and Resulting Stress Changes on Regional Faults, Bull. Seis. Soc. Am.,  
1112 103, 2326–2343, doi:10.1785/0120120306, 2013.

1113 Tanyaş, H., Westen, C. J., Allstadt, K. E., Jessee, M. A. N., Görüm, T., Jibson, R. W., Godt, J. W., Sato,  
1114 H. P., Schmitt, R. G., Marc, O., and Hovius, N.: Presentation and Analysis of a Worldwide Database of  
1115 Earthquake-Induced Landslide Inventories, J. Geophys. Res. Earth Surf., 122, 1991–2015,  
1116 doi:10.1002/2017jf004236, 2017.



1117 Tanyas, H., Rossi, M., Alvioli, M., Westen, C. J. van, and Marchesini, I.: A global slope unit-based  
1118 method for the near real-time prediction of earthquake-induced landslides, *Geomorphology*, 327, 126–  
1119 146, doi:10.1016/j.geomorph.2018.10.022, 2019a.

1120 Tanyaş, H., Westen, C. J., Allstadt, K. E., and Jibson, R. W.: Factors controlling landslide frequency–area  
1121 distributions, *Earth Surf Processes*, 44, 900–917, doi:10.1002/esp.4543, 2019b.

1122 Tanyaş, H., and Lombardo, L.: Variation in landslide-affected area under the control of ground motion  
1123 and topography, *Eng. Geol.*, 260, 105229, doi:10.1016/j.enggeo.2019.105229, 2019.

1124 Tanyaş, H., Görüm, T., Fadel, I., Yıldırım, C., and Lombardo, L.: An open dataset for landslides triggered  
1125 by the 2016 Mw 7.8 Kaikōura earthquake, New Zealand, *Landslides*, 19, 1405–1420,  
1126 doi:10.1007/s10346-022-01869-9, 2022.

1127 Von Hillebrandt-Andrade, C., and Vanacore, E.: Citizen science for studying earthquakes, *Science*, 376,  
1128 246–247, <https://doi.org/10.1126/science.abo5378>, 2022.

1129 Wartman, J., Dunham, L., Tiwari, B., and Pradel, D.: Landslides in Eastern Honshu Induced by the 2011  
1130 Tohoku Earthquake Landslides in Eastern Honshu Induced by the 2011 Tohoku Earthquake, *Bull. Seis.  
1131 Soc. Am.*, 103, 1503–1521, <https://doi.org/10.1785/0120120128>, 2013.

1132 Wilson, R.C., and Keefer, D.K.: Predicting the areal limits of earthquake-induced landsliding, In  
1133 *Evaluating Earthquake Hazards in the Los Angeles Region - An Earth Science Perspective* (Ziony, ed.),  
1134 U.S. Geol. Surv. Prof. Paper 1360, 316-345, 1985.

1135 Xu, C., Shyu, J. B. H., and Xu, X.: Landslides triggered by the 12 January 2010 Port-au-Prince, Haiti,  
1136 Mw = 7.0 earthquake: visual interpretation, inventory compiling, and spatial distribution statistical  
1137 analysis, *Nat. Hazards Earth Syst. Sci.*, 14(7), 1789–1818, doi:10.5194/nhess-14-1789-2014, 2014.

1138 Zhao, B., Wang, Y., Li, W., Lu, H., and Li, Z.: Evaluation of factors controlling the spatial and size  
1139 distributions of landslides, 2021 Nippes earthquake, Haiti, *Geomorphology*, 415, 1-16,  
1140 [doi.org/10.1016/j.geomorph.2022.108419](https://doi.org/10.1016/j.geomorph.2022.108419), 2022.

1141

1142

1143

**Formatted:** Font: (Default) Times New Roman, 10 pt

**Formatted:** Font: (Default) Times New Roman, 10 pt

**Formatted:** Normal, Space After: 0 pt, Line spacing: single

**Formatted:** Font: (Default) Times New Roman, 10 pt, English (United States)

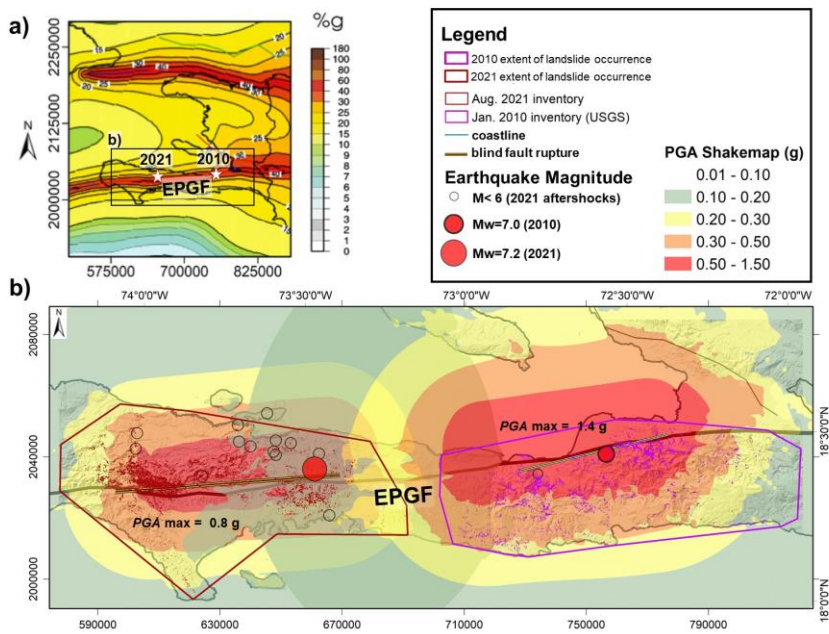
**Formatted:** Font: (Default) Times New Roman, 10 pt, English (United States)

**Formatted:** Font: (Default) Times New Roman, 10 pt

**Formatted:** Check spelling and grammar

1144  
1145  
1146  
1147  
1148  
1149  
1150  
1151  
1152

Annex



1153  
1154  
1155  
1156

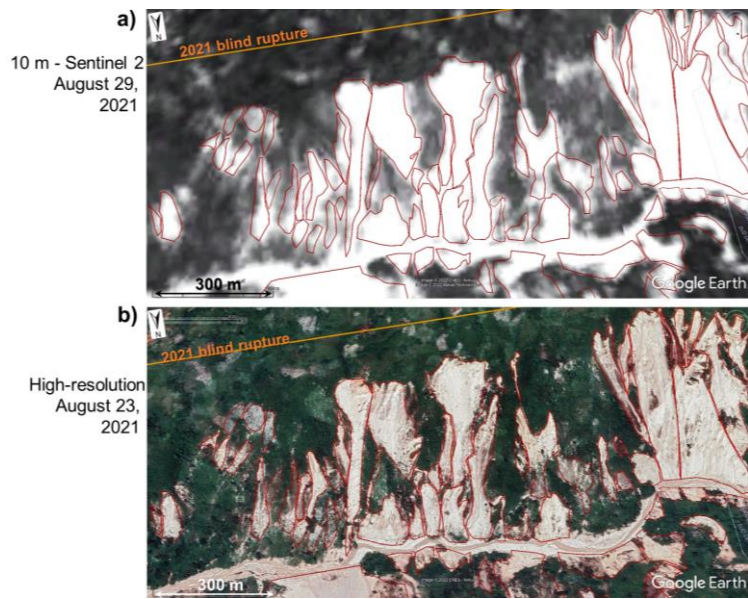
Figure A1: a) Seismic hazard map of Haiti (modified from Frankel et al., 2011) with location of the January 12, 2010, and August 14, 2021, main epicenters. b) Combined overlays of shakemaps of the 2010 (right part of map) and 2021 (left part) earthquakes.

1157

1158

1159

1160

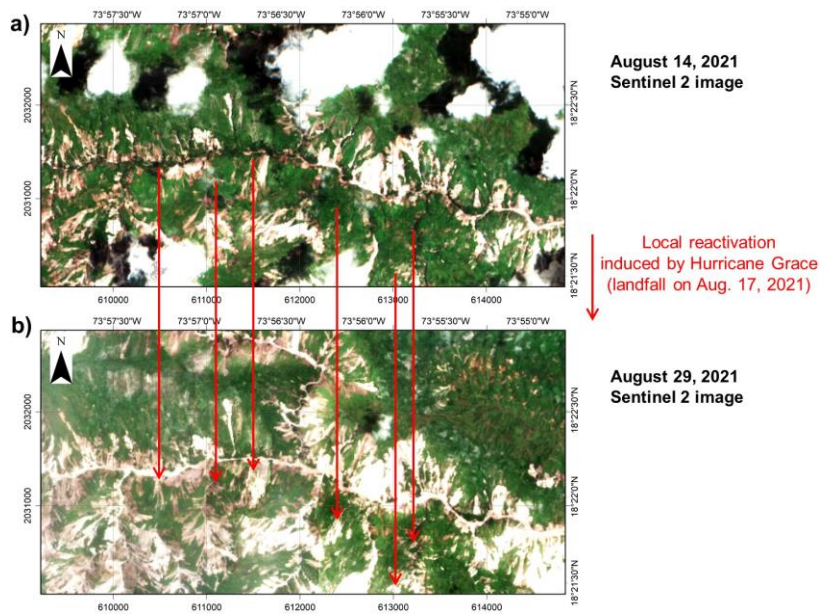


1161

1162 **Figure A2: Comparison between (a) a Sentinel-2 image (10-m resolution) and (b) a high-resolution (~0.5-1 m)**

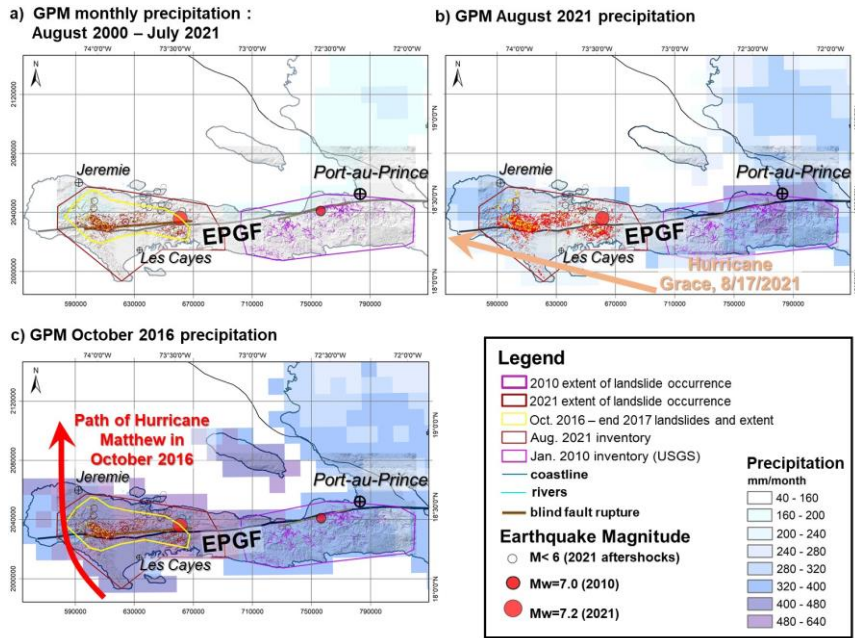
1163 **image (© Google Earth) of the same area affected by landslides triggered by the earthquake event in August**

1164 **2021.**



1165

1166 **Figure A3: Comparison between Sentinel-2 images (10-m resolution) for the same area obtained for (a) August**  
 1167 **14 (about 2h after the main shock) and for (b) August 28, 2021 (12 days after impact by Hurricane Grace that**  
 1168 **crossed the region on August 16, 2021). Red arrows point to zones where an intensification of denudation and**  
 1169 **sliding can be observed.**



1170

1171 **Figure A4: Monthly © Global Precipitation Measurement Mission (NASA) maps (0.1° resolution, values in**  
 1172 **mm/month) for southwestern Haiti, (a) for all months between August 2000 and July 2021, (b) for August**  
 1173 **2021 (marked by the Hurricane Grace event), and (c) for October 2016 (marked by the Hurricane Matthew**  
 1174 **event).**

1175